Proximity effect in topological insulator/superconductor heterostructure

He Jia-Dian [1,2*], Ding Yi-Fan [1,2*], Teng Bo-Lun [1,2], Dong Peng [1,2], Li Yi-Fei [1,2], Zhang Yi-Wen [1,2], Wu Yue-Shen [1,2], Wang Jing-Hui [1,2], Zhou Xiang [1,2†], Wang Zhi [3], Li Jun [1,2‡]

1. School of Physical Science and Technology, ShanghaiTech University, Shanghai 200031, China
2. ShanghaiTech Laboratory for Topological Physics, ShanghaiTech University, Shanghai 200031, China
3. School of Physics, Sun Yat-sen University, Guangzhou 510275, China

Abstract: Topological superconductors have attracted increasing attentions for the purpose of the quantum computation, because the character of supporting topological qubits are immune to quantum decoherence and can be manipulated by braiding operation. Since the topological superconducting state is rather rare in the intrinsic topological superconductors, most of experimental efforts focus on inducing topological superconductors by the proximity effect in superconductor (SC)/topological insulator (TI) heterostructures. Fu and Kane have theoretically proposed that the topological superconductivity can be obtained by inducing an s-wave superconducting gap into TIs. After that, a lot of experimental progress has been made in different systems. In the first part of this review, we introduce the heterostructure of three-dimensional (3D) TI Bi_2Se_3 and Bi_2Te_3 on s-wave SC $NbSe_2$ and d-wave SC $Bi_2Sr_2CaCu_2O_{8+\delta}$, topological crystalline insulator $Sn_{1-x}Pb_xTe$ on Pb, two-dimensional (2D) TI WTe_2 on $NbSe_2$, and $TiBiSe_2$ on Pb. In the second part, the TI-based Josephson junctions are reviewed by introducing various experiments, including the Josephson junctions with TI barrier layers based on the Fu-Kane mode, and the superconducting quantum interference devices by TI based Josephson junctions.

Key words: proximity effect; topological superconductor; heterostructure; Josephson junction

CLC number: O469 **Document code:** A **DOI:** 10.13725/j.cnki.pip.2021.03.001

CONTENTS

Received date: 2021-1-8
* These authors contributed equally to this work.
† E-mail: zhouxiang@shanghaitech.edu.cn
‡ E-mail: lijun3@shanghaitech.edu.cn

I. INTRODUCTION

Quantum computation is widely believed as a highly potential path to solve the quantum limit in conventional computation technique[1–4]. However, the quantum decoherence which destroys the quantum information storage of a qubit and the entanglement between qubits is still the major challenge to realize quantum computation. Theoretically, topological superconductors (TSCs) are supposed to be a possible way to solve this problem. TSCs host bizarre quasiparticles called Majorana zero modes (MZMs), whose antiparticles are themselves[5–10]. MZMs obey non-Abelian statistics, and can construct qubits which are naturally immune to quantum decoherence, providing an ideal route to achieve fault-tolerant quantum computation.

As a TSC, the wavefunction should keep a nontrivial topological nature and the pair potential should be anisotropic, for instance, a spinless p-wave superconductor. Sr_2RuO_4 was considered as a promising intrinsic TSC because it is an intrinsic p-wave superconductor with a chiral order parameter[11,12]. However, some recent studies demonstrated that Sr_2RuO_4 seems unlike a chiral p-wave superconductor[13]. Apart from the intrinsic mechanism, TSCs can be obtained by doping metallic elements into topological insulators (TIs), such as $Cu_xBi_2Se_3$[14], $Sr_xBi_2Se_3$[15], and $Nb_xBi_2Se_3$[16], and even from the vortex core in Fe-based high temperature superconductor of Fe(Te, Se)[17]. Besides, Fu and Kane predicted an alternative way to obtain TSC states by constructing a heterostructure of an s-wave superconductor and a TI[1], which is more practical for experimental realization.

The key point of the Fu-Kane mode is to induce an s-wave superconducting gap in the TI by the proximity effect. Chalcogenides are popular candidates for TIs, such as Bi_2Se_3[18], $TiBiSe_2$[19] and WTe_2[20]. However, the proximity effect induced superconducting wavefunction in the TI is degradated and sensitive to the interfacial electronic state. Thus, an ideal interface between the TI and the s-wave superconductor is essential to obtain a TSC.

In this article, we review the recent progress on realizing TSCs by the proximity effect. In Section II, we briefly introduce the background of TSCs, including the general behaviors of the TI, the TSC, and the MZM. Section III enumerates several experimental evidences about the proximity effect induced TSCs in TI/superconductor heterostructures, including Bi_2Se_3 / $NbSe_2$, Bi_2Te_3 / $NbSe_2$, WTe_2 / $NbSe_2$, Bi_2Se_3 / $Bi_2Sr_2CaCu_2O_{8+\delta}$, $Sn_{1-x}Pb_xTe$ / Pb and $TiBiSe_2$ / Pb heterostructures. Section IV is devoted to introduce the superconductor-TI-superconductor (S-TI-S) Josephson junctions based on (i) the Fu-Kane system, (ii) the quantum well and (iii) the two-dimension electron gas (2DEG), as well as the TI-based superconducting quantum interference device (SQUID).

II. BACKGROUND

A. Topological insulator

Firstly, we would like to briefly introduce the TI. In condensed matter systems, the spontaneously symmetry-broken is generally believed as the principle to classify states of matter according to the quantum field theory, such as solids, magnets and superconductors. In 1980s, as the discovery of integer quantum Hall effect (IQHE) and fractional quantum Hall effect (FQHE), the concept of topology ordering which originated from a mathematical concept to study the continuous deformation of geometric shapes or spaces, was introduced into condensed matter physics, and opened a new area in condensed matter physics[21,22]. Differing from the traditional states of matter mentioned above, the quantum Hall (QH) state does not break any symmetry and its properties depend on the global topology rather than the specific local order.

Over the past 40 years, the study of QH state has led to a new classification paradigm based on the topological order[23], which is originally raised to characterize the intricately correlated QH states[22,24]. In these regards, the simplest QH system is the integer QH states, which can be understood within the framework of the band theory. Figure 1(a) describes the electronic structure of a conventional insulator. Due to the pinning effect of the outer electrons by their atoms, the valence band and conduction band are divided by an

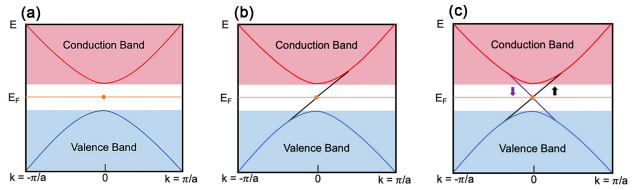

FIG. 1. The illustrations of band structures of a (a) normal insulator, (b) quantum Hall insulator and (c) quantum spin Hall insulator.

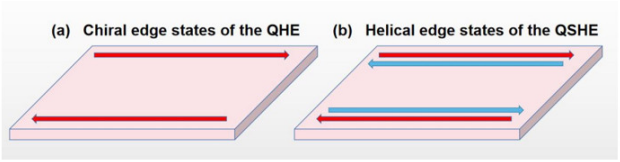

FIG. 2. The illustrations of (a) chiral edge states of the quantum Hall effect and (b) helical edge states of the quantum spin Hall effect. The arrows represent the directions of current and different colors represent different orientations of spin.

energy gap, which the electrons can hardly overcome directly. While for the QH insulator, the outer electrons are pinned by the applied magnetic field, which opens an energy gap and leads to an insulating bulk state. However, due to the bounced cyclotron orbits in the edge, the electrons can skipping motion along the edge, resulting in a single edge or surface state which connects the valence band and conduction band, as can be seen in Fig. 1(b).

The simplest QH system is the IQHE, which always appears in a 2DEG under strong magnetic field and low temperature[21]. In this case, the electrons move along quantized circular orbits under the external magnetic field, leading to quantized Landau levels. As a consequence, the Hall conductance is quantized as well, which could be written as:

$$\sigma_{xy} = ve^2/h \tag{1}$$

where, v could be an integer or a fraction, which corresponds to IQHE and FQHE, respectively. Thouless et al. explained the differences between the QH state and normal insulator by using the concept of topology, and found that v is identical to the Chern invariant n [10,24]. The topological invariant of QH state will change on the boundary, which is different from the normal insulators. In this case, the boundary forms some non-dissipative edge states. The electrons in the edge will move in the chiral edge states protected by topological phase as given in Fig. 2(a). It should be noted that magnetic field will break time-reversal symmetry in the system.

In 2005, Kane and Zhang[25,26] predicted the realization of quantum Hall effect (QHE) under zero magnetic field through the inherent strong spin-orbit coupling in 2D TI respectively, which is named as quantum spin Hall effect (QSHE). Kane and Mele[25,27] raised an effective way to obtain the QSHE state in converted graphene from an ideal two-dimensional (2D) semimetalic state by a spin orbit potential. Similar to the QHE, the QSHE is gapped in the bulk, while due to the gapless edge states, both spins and charges can propagate at the boundaries, as shown in Fig. 1(c). However, the edge states are non-chiral, but insensitive to nonmagnetic disorder due to their correlated spin orientations.

Since the QSHE originates from strong spin-orbit coupling, it can be protected by time reversal symmetry and does not require a strong magnetic field. The degree of freedom between the spin angular momentum and the orbit angular momentum will couple together and form a helical edge state. The band will be bended inside the crystal, and electrons will be controlled by a spin-dependent force. When there is a current, the electrons with opposite spin will flow along the opposite directions at the edges but the net current is not zero, as shown in Fig. 2(b). If the TI is a ferromagnet, the magnetic ordering can break the time reversal symmetry and open a gap at the Dirac point of the surface states. In this case, ferromagnetism can suppress one spin channel in the QSH system. Thus only one spin current is permitted to propagate at the edge, which is different from the normal QSH state. This is a time reversal symmetry-breaking state of matter which is closely related to the QSHE, called the quantum anomalous Hall effect (QAHE). In 2013, Chang et al. experimentally observed the QAHE in chromium-doped (Bi, Sb)$_2$Te$_3$ thin films for the first time, which confirms the prediction that the QAHE occurs in magnetic TIs[28].

B. Proximity effect of superconductivity

When two different materials are connected to each other, the phase coherence of wavefunction may penetrate from one material into another and induce new properties, which is called the proximity effect. Assuming when a non-superconductor (Non-SC) is attached to a superconductor (SC) through a highly transparent interface, as shown in Fig. 3, the superconducting order parameters of the SC (Δ_s) near the interface (about a distance of ξ_s) is suppressed, while the order parameters of Non-SC is induced to a nonzero value near the interface with a penetration depth of ξ_N. Thus, there are basically two intermediate regions: 1) the weakened superconductivity properties of the SC, and 2) an induced finite superconductivity state in the Non-SC. This is the so-called superconducting proximity effect. Particularly, the induced superconductor in the Non-SC is of great interest because it provides a possibility to obtain a TSC, which has been predicted by Fu and Kane[2].

TSCs are fascinating because the induced 2D superconductor is no longer a s-wave superconductor. Since the surface states are spin non-degenerate and only contain half the degrees of freedom of a normal metal, the induced TSC states are similar to the spinless $p_x + ip_y$ superconductors[29–31]. Thus, the surface superconductor should host zero energy Majorana state bounds (MSBs) at vortex core[2]. The detailed information for the proximity effect induced TSCs will be discussed in the following subsections.

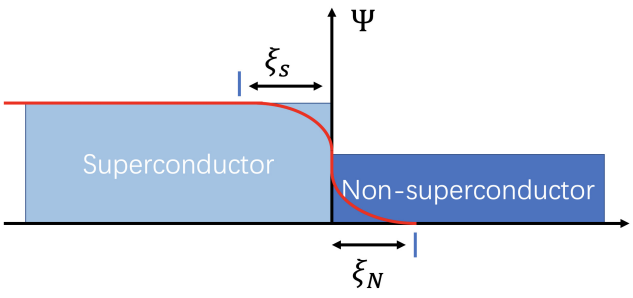

FIG. 3. The schematic of the hetero-junction between a superconductor and a non-superconductor. The red line represents the superconducting wave function.

C. Topological superconductors

TSCs have a close connection to the orbital symmetry of gap functions, which corresponds to the relative orbital momentum of electrons to form a Cooper pair. Figure 4 shows the potential energy near Fermi surface with different orbit symmetries in 2D cases. There are two types of spin symmetries for pair potential: spin-singlet and spin-triplet. Symmetries of the orbit and spin parts will be combined together to keep the anti-symmetric nature of pairing functions. Whether the s-wave superconductor or the d-wave superconductor are spin-singlet, while the p-wave superconductor (Sr_2RuO_4[32,33]) and f-wave superconductor (UPt_3[34]) are spin-triplet.

The pair potentials with different orbits have different numbers of nodes. Thus, the topological nature can be characterized by topological number in one-dimensional systems. The topological number is an integer and nonzero coefficient corresponding to the nontrivial phase of superconductor, which is constant when energy gap is opened at the Fermi level. That is, a non-zero topological number suggests a nontrivial edge state at the surface of topological superconductor.

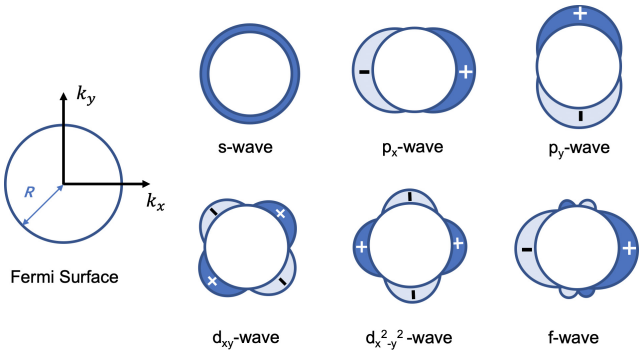

FIG. 4. Pair potentials on a two-dimensional Fermi surface.

When a TI is connected with an s-wave superconductor, an effective chiral p-wave superconductivity can be induced at the TI/SC interface. Since chiral p-wave superconductor characterizes a topological number of "1", the topological number will be modified from "0" to "1" at the TI/SC interface, so the gapless energy states near Fermi surface must exist at the interface. Meanwhile, the number of zero-energy states in the interface is consistent with the change of topological

number.

D. Majorana zero mode

In the TSC, one of the most unique characters is the fully superconducting gap but with topologically protected Majorana state[35]. The Majorana fermions whose antiparticle is itself, was firstly proposed by Majorana in 1937[36]. Researches on MZM are extremely hot in condensed matter physics because it is a promising candidate for topological quantum computation. Since the Majorana fermions can only exist in the vortices or boundaries of TSCs, the realization of TSCs is the key issue to create and manipulate MZMs[37,38].

As the simplest non-Abelian excitation, MZMs would have profoundly technological applications for topological quantum computation[5–7,36]. According to the theoretical prediction, MZMs are associated with the spinless $p_x + ip_y$ superconductor, including the quasiparticle excitations of the $\nu = 5/2$ quantum Hall effect[5,31,39], Sr_2RuO_4[33], cold fermionic atoms[4,40] and 2D structures combined with superconductivity, magnetism, and strong spin-orbit coupling[41,42]. Besides, MZMs can be created at the interface between strong TIs and s-wave superconductors, which is easier to be detected and manipulated experimentally.

E. The Fu-Kane mode

Compared with the ordinary insulator, the crucial feature of the TI is the surface state, whose Fermi circle encloses an odd number of degenerate Dirac points and is associated with a π Berry phase. Considering the simplest case, with a single non-degenerate Dirac point, the time reversal invariant Hamiltonian can be described as:

$$H_0 = \psi^\dagger(-iv\vec{\sigma}\cdot\nabla - \mu)\psi \tag{2}$$

Here, $\psi = (\psi^\dagger, \psi)^T$ is the electron field operator, $\vec{\sigma} = (\sigma^x, \sigma^y)$ is the Pauli spin matrix, μ is the chemical potential energy. Since the Hamiltonian H_0 violates the fermion doubling theorem[43], it can only exist on a surface.

Suppose there is a superconductor contacting with this TI, the cooper pairs can tunnel into the surface

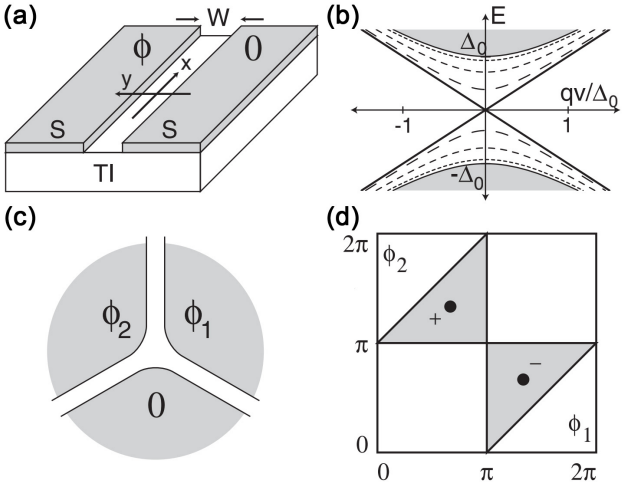

FIG. 5. (a) Schematic of the S-TI-S junction. (b) Dispersion spectrum of the S-TI-S junction in (a). (c) Schematic of the tri-junction between three superconductors, TI is lying under the superconductors. (d) Phase diagram of the tri-junction[2]. Copyright ©2008, American Physical Society.

states due to the proximity effect, which means an additional energy term add to the surface state:

$$V = \Delta\psi_\uparrow^\dagger\psi_\downarrow^\dagger + h.c. \tag{3}$$

Here, $\Delta = \Delta_0 e^{i\phi}$ depends on the nature of the surface, and ϕ is the phase of the superconductor[44]. Then, the surface states can be written by:

$$H = \Psi^\dagger\mathcal{H}\Psi/2 \tag{4}$$

$\mathbf{\Psi} = ((\psi_\uparrow, \psi_\downarrow), (\psi_\downarrow^\dagger, -\psi_\uparrow^\dagger))^T$ is the Nambu notation, and

$$\mathcal{H} = -iv\sigma\tau^z\cdot\nabla - \mu\tau^2 + \Delta_0(\tau^x\cos\phi + \tau^y\sin\phi), \tag{5}$$

where $\vec{\tau}$ is a Pauli spin matrix that mixes ψ and $\psi^\dagger$.

Fu and Kane[2] proposed a line Josephson junction which consists of two superconductors with phase 0 and π, and a TI barrier layer, as shown in Fig. 5(a). The width of the junction is W and the length is $L \to \infty$. The Andreev bound states in the surface state channel between the superconductors were analyzed by solving the Bogoliubovde Gennes (BdG) equation $\mathcal{H}\xi = E\xi$ with $\Delta(x, y) = \Delta_0 e^{i\phi}$ for $y > W/2$, Δ_0 for $y < -W/2$ and 0 otherwise. For $W = \mu = 0$, the energy spectrum can be described by:

$$E_\pm(q) = \pm\left[v^2q^2 + \Delta_0^2\cos^2(\phi/2)\right]^{1/2} \tag{6}$$

For $\phi = \pi$, the spectrum is gapless. With decreasing ϕ, an energy gap emerges and the bound states merge with the continuum for $\phi = 0$, as shown in Fig. 5(b).

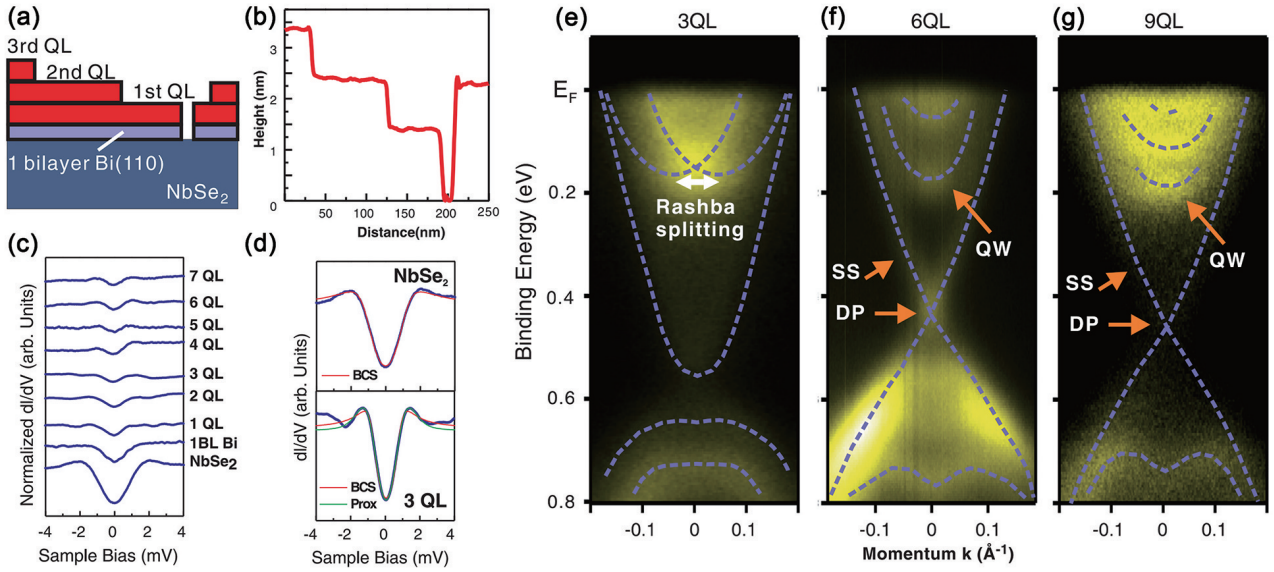

FIG. 6. Measurement of superconducting gap and energy band on Bi_2Se_3/Nb_2Se_3 heterostructure. (a) Schematic of Bi_2Se_3 film grown on Nb_2Se_3. (b) Height profile of Bi_2Se_3 along a line in the Bi_2Se_3 film. (c) Evolution of induced superconducting gaps as the layer of Bi_2Se_3 film increases. (d) Top panel is the dI/dV spectrum of bared $NbSe_2$ and corresponding BCS theory fitting. Bottom panel is the dI/dV spectrum of 3-QL Bi_2Se_3 film affected by $NbSe_2$ and corresponding BCS theory fitting. Figure (e) (f) and (g) are energy spectra of 3-QL, 6-QL and 9-QL Bi_2Se_3 films grown on Nb_2Se_3,respectively. Energy spectra is acquired by ARPES measurement[50]. Copyright ©2012, Science.

While for a tri-junction, in which three superconductors are divided by line junctions meet at one point, as shown in Fig. 5(c), the MBSs will exist under certain conditions. The phase diagram in Fig. 5(d) is deduced by solving the BdG equation with special limits. When $\phi_{k=1,2} = 0$, there is no bound state. However, when three line junctions are oriented at 120°, which means $\phi_k = \pm k(2\pi/3)$, and the ± MBSs are found for $\mu = 0$. Moreover, the MBSs will not disappear until the phase difference between two neighboring superconductors is π. The shadow regions in Fig. 5(d) represent the MBSs occur in the phase diagram.

Topological Josephson junction or SC/TI heterostructure based on proximity effect has attracted a lot of attention since Fu-Kane mode was proposed. It provided a vast platform to find MZM. Up to now, creating TSCs via proximity effect have extensively applied in 2DEG systems and Weyl semimetals[45–47]. Many reports proposed that topological edge states existed in such systems and could be tuned by gate voltage or magnetic field[19,48,49]. These systems are also in great potential to create and manipulate MZM, which needs more detailed investigations in the future.

III. TOPOLOGICAL INSULATOR/SUPERCONDUCTOR HETEROSTRUCTURES

As introduced in the Fu-Kane mode in section II, TSCs can be induced by the TI/SC heterostructures, while both the TI and the SC can be substituted. The ideal superconductor is $NbSe_2$, which shows a typical *s*-wave pairing symmetry. More importantly, the high quality single crystal with 2D structure reinforces superior in the heterostructure and even device fabrications. Other superconductors like $Bi_2Sr_2CaCu_2O_{8+\delta}$ can also be applied in the heterostructures.

A. Hybrid junctions of topological insulators and *s*-wave superconductors

1. Heterostructure of $Bi_2Se_3/NbSe_2$

Bi-based TI materials, such as Bi_2Se_3, Bi_2Te_2 and $Bi_{1-x}Sb_x$[10], are known as the 3D TIs, which have various desirable properties. Therefore, Bi-based TIs are appropriate candidates to realize TSCs.

In 2012, Wang *et al.*[50] reported the observation

of TSC in single-crystalline Bi_2Se_3 thin films grown on 2H-$NbSe_2$ (0001) by molecular beam epitaxy (MBE). Figure 6(a) shows the schematic of $Bi_2Se_3/NbSe_2$ heterostructur, and Fig. 6(b) reveals the height profile extracted from the scanning tunneling microscopy (STM) image, which is perfectly corresponding to the design.

Figure 6(c) shows the evolution of superconducting gap-like dI/dV spectra with the Bi_2Se_3 thickness increasing, which indicates that the induced superconducting gap decreases rapidly as the thickness of Bi_2Se_3 film increases. Such evolution is in consistent with the proximity effect. The upper panel of Fig. 6(d) displays the dI/dV spectrum of bared $NbSe_2$ at 4.2 K, from which a superconducting gap of about 1.1 meV can be obtained since the spectrum is identical with the Bardeen-Cooper-Schrieffer (BCS)-like tunneling spectrum function (labeled as red solid line). Nevertheless, neither the BCS function nor the simple proximity effect function can fit the spectrum of 3-quintuple layers (QL) Bi_2Se_3 film very well, although both of them can give a roughly similar gap size (seen as Fig. 6(d), lower panel).

The energy band dispersions of Bi_2Se_3 with different thicknesses measured by ARPES are shown in Figs. 6(e-g). Obviously, the Dirac point emerges when the thickness is no less than 6 QL. For the 3 QL Bi_2Se_3 film, an energy gap opens at the binding energy is approximate 0.6 eV. Besides, the energy band splits due to the Rashba spin-orbital coupling at the binding energy of 0.15 eV (Fig. 6(e)), which is not observed for thicker samples, indicating the weak electric field on the surface. Meanwhile, the energy gap disappears and a Dirac point (labeled as DP in Figs. 6(f-g)) emerges, revealing the decoupling of the surface and interface. The quantum-well like state (labeled as QW in Figs. 6(f-g)) is also observed in this system. Similar phenomena are observed in the thicknesses of 9 OL and 12 QL.

The observation of superconducting gap and Dirac point at the topological Bi_2Se_3 surface by both STM spectra and ARPES provides a direct evidence about the coexistence of superconductivity and topological order. The coexistence of the superconducting gap and topological surface states in $Bi_2Se_3/NbSe_2$ heterostructure make it a promising platform to study the unusual properties of the topological ordered superconductors, and to detect MZMs[51].

Growing TI films on superconductor substrate is widely used for STM and ARPES measurement. Normally, if the thickness of TI film is too thin, two surfaces (SC/TI interface and TI/vacuum interface) will couple together and Dirac point will disappear. When the thickness of TI film is appropriate, superconducting gap can be induced into top surface (TI/vacuum interface) and coexist with surface state. MZM is predicted to exist in the vortex core of both surfaces, which can be directly probed by STM.

2. Heterostructure of $Bi_2Te_3/NbSe_2$

In 2015, Sun *et al.*[52] reported the observation of MZMs in the vortex core of 5QL-$Bi_2Te_3/NbSe_2$ heterostrusture with spin-polarized STM/STS measurement. The measurement is based on the spin-selective Andreev reflection (SSAR) of MZMs, which is a direct and convincing evidence of MZMs.

SSAR is initially proposed in 1D systems[53]. When an electron is propagating from a superconducting lead to a non-superconducting lead, it will be reflected as a counter-propagating hole with the same spin orientation at the interface[2], which is known as the Andreev reflection. Since the vortex induced by the applied magnetic field is quite small in the TSC, the polarization of surface states and finite-energy quasiparticle states could be neglected in STM/STS measurement. Figure 7(a) depicts a vortex core on the surface of $Bi_2Te_3/NbSe_2$. The size of vortex core is about 80 nm. In the vortex core, the direction of spin polarization (SP) is consistent with the external magnetic field. When the SP of the tip is parallel to the external magnetic field, zero-energy electrons will be reflected as counter-propagating holes and lead to a high zero bias conductance. When the SP of the tip is antiparallel to the external magnetic field, zero-energy electrons will be reflected directly and lead to a low zero bias conductance, as shown in Fig. 7(b). The tunneling conductance difference between parallel and antiparallel situations is about 14%. Figure 7(c) indicates that dI/dV is independent of spin orientation outside the vortex core, which is a vital evidence to prove the existence of MZMs in vortex core.

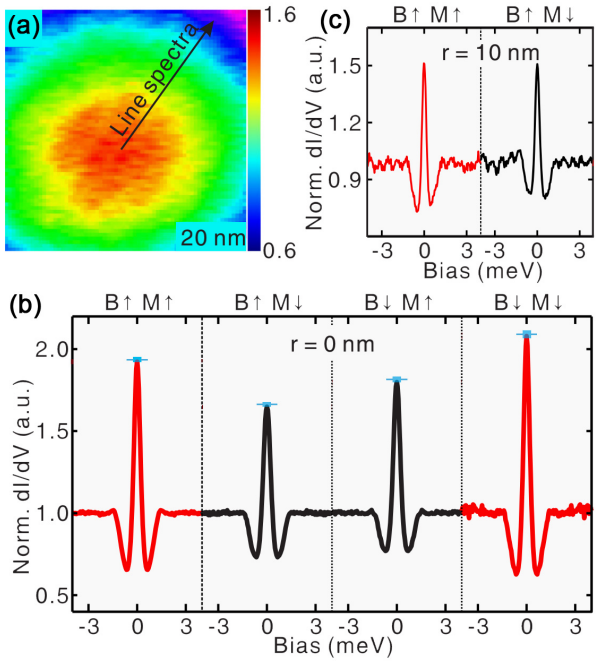

FIG. 7. STM/STS measurements performed at 30 mK and 0.1 T magnetic field. (a) Zero bias dI/dV mapping of the vortex core on 5QL $Bi_2Te_3/NbSe_2$ measured by spin polarized tip. (b) dI/dV curves in vortex core measured by spin polarized tip. Red curve represents that the SP of tip is parallel to external magnetic field and black curve corresponds to the antiparallel situation. dI/dV curve is normalized to the dI/dV value outside of superconducting gap for comparison. (c) dI/dV curves at 10 nm away from vortex core[52]. Copyright ©2016, American Physical Society.

Since the splitting energy between MZMs and other low-lying vortex core bound states is proportional to the square of the induced superconducting gap[54], lots of efforts have been spent on finding new SC/TI systems with larger induced superconducting gap to detect MZM by STM[20,50,55]. This work takes use of the unique magnetic property of MZMs (SSAR) and successfully differentiates MZMs from other vortex core bound states. It is suggested that spin-resolved techniques can also be applied into other systems for detecting and manipulating MZMs[53,56,57].

3. Heterostructure of $WTe_2/NbSe_2$

Although it has been realized in epitaxial 3D TI films grown on superconducting substrates[50,52], the exploration of topological superconductivity in van der Waals materials is more practical on devices fabrication. The unique stack structure of van der Waals materials will induce 2D quantum spin Hall edges in vertical heterostructures, which allowing the probe and investigation of 1D topological superconducting states.

Soon after the theoretical prediction[58], the intrinsic quantum spin Hall state has been experimentally demonstrated in monolayer WTe_2[59–61], providing a excellent platform to investigate quantum spin Hall edge modes in van der Waals heterostructures. Moreover, the monolayer WTe_2 was reported to be intrinsic superconducting when it was gated to the conduction band, and the critical temperature (T_c) is about 1 K[62,63]. In this way, the monolayer WTe_2 is an appropriate candidate to realize TSC. The remaining question is to improve T_c. Quite recently, Lüpke et al.[20] reported the coexistence of superconducting gap and the quantum spin Hall signal at the edge of the monolayer WTe_2 when they transferred the monolayer WTe_2 onto the van der Waals s-wave superconductor $NbSe_2$. It is encouraging that this approach is free of electrostatic doping and T_c is much higher than the intrinsic one. They attributed this improvement to the proximity effect.

Figure 8(a) represents the schematic of the sample structure and measurement setup. The dI/dV spectra of the $NbSe_2$ (blue line) and the WTe_2 monolayer (red line) are shown in Fig. 8(b). Apparently, similar to the superconducting $NbSe_2$, the WTe_2 monolayer reveals a superconducting gap-like spectrum, which is characterized by a dip at the Fermi energy, and two peaks on either sides. Moreover, both the monolayer WTe_2 and the $NbSe_2$ spectra can be fitted by the BCS model, labeled as black dash lines in Fig. 8(b), and the fitted superconducting energy gaps are 0.72 ± 0.02 meV and 0.84 ± 0.01 meV, respectively. To have a more detailed theoretical analysis, a contrast experiment is performed to isolate the respective contributions of WTe_2 and $NbSe_2$, as shown in Fig. 8(c).

Figure 8(d) represents a typical tunneling spectrum of the $WTe_2/NbSe_2$ heterostructure. The gray and maroon dash lines indicate the superconducting gap of $NbSe_2$ and proximity-induced that of WTe_2. All spetra can be fitted by BCS model very well, and the size of the induced gap are 0.76 ± 0.16 meV at 4.7 K and 0.83 ± 0.08 meV at 2.8 K. Following the similar procedure, the induced superconducting gap of the WTe_2

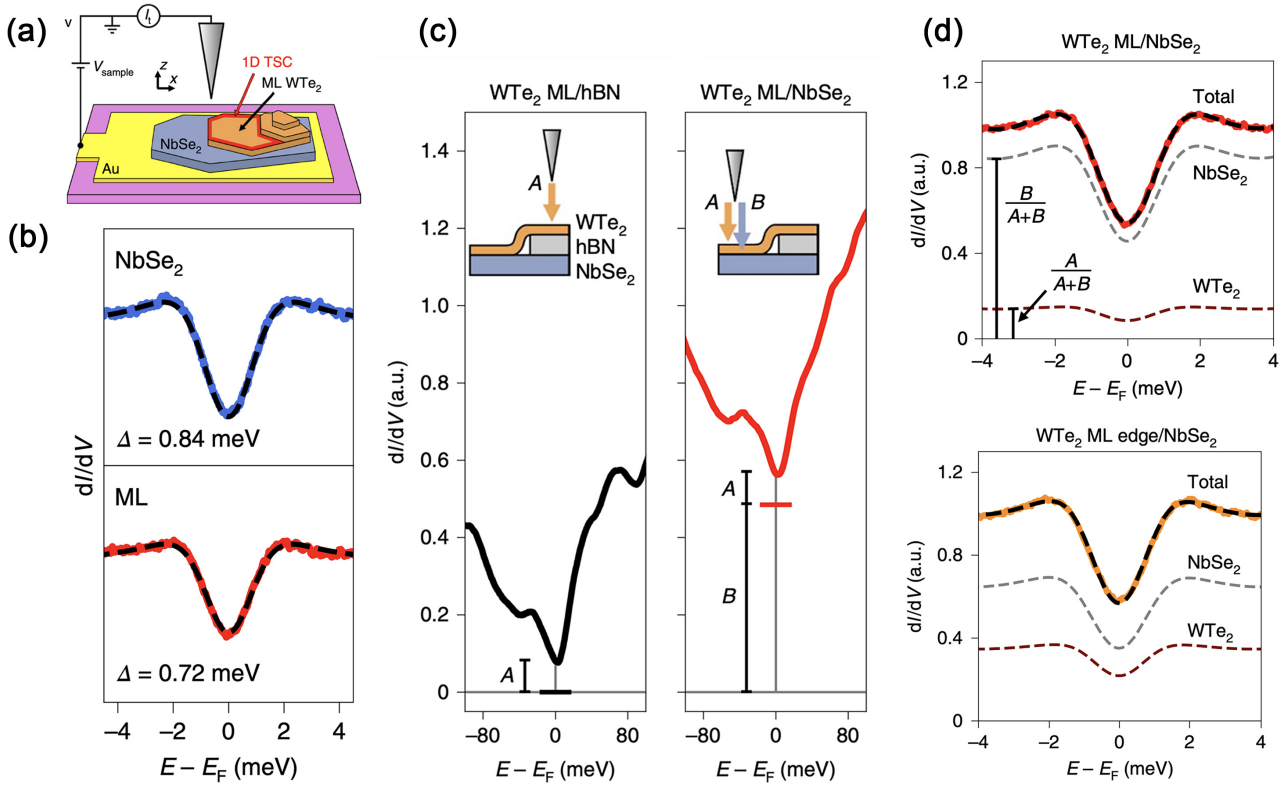

FIG. 8. Measurement of induced superconducting gap in monolayer WTe_2. (a) Schematic of $WTe_2/NbSe_2$ heterostructure. (b) The top panel is BCS theory fitted intrinsic superconducting gap on $NbSe_2$, the bottom panel is BCS theory fitted induced superconducting gap on monolayer WTe_2. (c) dI/dV spectra of monolayer WTe_2 on $NbSe_2$ and on hBN for comparison. The tunneling contributions of the WTe_2 and $NbSe_2$ are denoted as A and B, respectively. (d) The top panel is BCS theory fitted dI/dV spectrum on monolayer $WTe_2/NbSe_2$, the bottom panel is BCS theory fitted dI/dV spectrum on monolayer WTe_2 edge/$NbSe_2$ [20]. Copyright ©2020, nature publishing group.

quantum spin Hall edge state is fitted to be 0.75 ± 0.08 meV. Moreover, by comparing the profile of induced superconducting gap spectra and the profile of quantum spin Hall edge state, it is apparent that the superconducting gap exists in the region where the quantum spin Hall edge state is observed.

The coexistence of superconducting gap as well as quantum spin Hall edge states strongly suggest the existence of 1D topological superconducting state in van der Waals heterostructure. If a boundary of the quantum spin Hall edge state is created, a topologically trivial gap will open and the MZM will localize at the boundaries. This may be realized by integrating a van der Waals magnetic insulator into this stacked $WTe_2/NbSe_2$ heterostructure to open a Zeeman gap. The work establishes a groundwork to realize Majorana quasiparticles in van der Waals materials.

B. Hybrid junctions of topological insulators and d-wave superconductors

$Bi_2Sr_2CaCu_2O_{8+\delta}$(BSCCO) is a typical d-wave high-temperature SC and its T_c is up to 90 K. Zareapour et al. to investigated the proximity effect in BSCCO/Bi_2Se_3 heterostructures by attaching a Bi_2Se_3 crystal onto a BSCCO base crystal [64]. Figure 9 shows the electric transport measurements of the BSCCO/Bi_2Se_3 interface along c-axis. The $I - V$ curves near T_c show a linear relation and a low resistance, indicating a good quality of BSCCO/Bi_2Se_3 interface. There are three superconducting gaps in the heterostructure: Δ_0, Δ_r and Δ_i, which correspond to the intrinsic superconducting gap, the reduced superconducting gap of BSCCO near interface, and the induced gap in Bi_2Se_3, respectively. When the tempera-

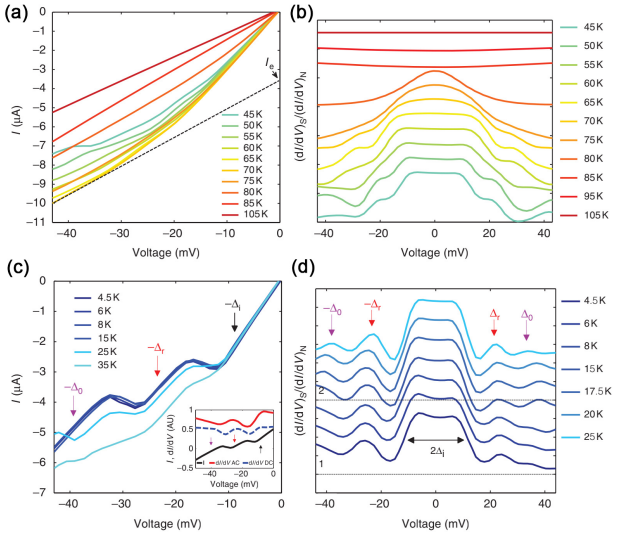

FIG. 9. (a) DC current-voltage relation of BSCCO/Bi_2Se_3 heterostructure in a temperature range passing through T_c. (b) AC differential conductance spectra measured in the same temperature range with figure (a), normalized by the differential conductance spectra of 105 K. (c) DC current-voltage relation of a low-resistance BSCCO/Bi_2Se_3 heterostructure far below T_c. (d) AC differential conductance of a low-resistance BSCCO/Bi_2Se_3 heterostructure measured in the same temperature range with figure (c), normalized by the differential conductance spectra of 105 K[64]. Copyright ©2012, nature publishing group.

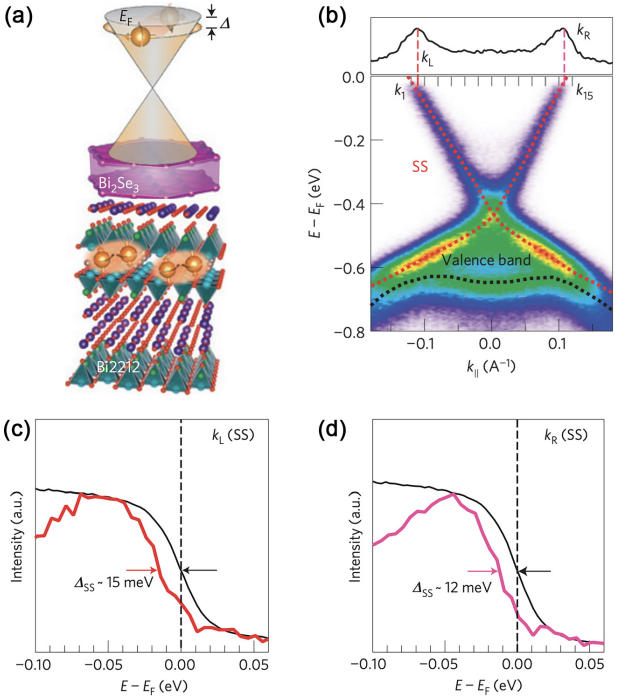

FIG. 10. (a) Schematic of BSCCO/Bi_2Se_3 heterostructure. (b) Upper panel is MDC curve integrated from 20 meV to -20 meV, bottom panel is ARPES measured at 20 K with phonon energy 50 eV. (c) and (d) are EDCs at Fermi momentums k_L and k_R in figure (b). EDCs in black are taken from a pure metal surface for comparison[54]. Copyright ©2013, nature publishing group.

ture is lower than 60 K, the features of Δ_i and Δ_r start to emerge. The kinks in $I-V$ curves and coherence peaks in differential conductance spectra are obvious at low temperature, as shown in Figs. 9(c) and 9(d). Particularly, an Andreev reflection effect induced zero-bias conductance peak in the range of $2\Delta_i$ is observed, as shown in Fig. 9(d).

In order to identify the induced superconducting states in Bi_2Se_3, Wang et al. performed the ARPES measurement of the MBE grown Bi_2Se_3 thin films onto the BSCCO substrate[54], which indicates a clearly linear dispersion of electrons around Dirac point, as shown in Fig. 10(b). The right and left Fermi vectors correspond to two peaks in momentum distribution curve(MDC). The shift of Fermi level may be caused by electric transforming from the BSCCO substrate. Under the condition of 50 eV phonon energy, the energy distribution curves (EDCs) will shift due to the existence of the energy gap in Bi_2Se_3 surface states, which is different from the standard EDCs in a pure metal surface. The energy gaps in different directions can be extracted from the shift in Figs. 10(c) and 10(d). According to the ARPES measurements, the induced gap on the surface states is rather isotropic(not shown in this paper). Thus, the *d*-wave superconductor induces a *s*-wave superconducting gap in Bi_2Se_3.

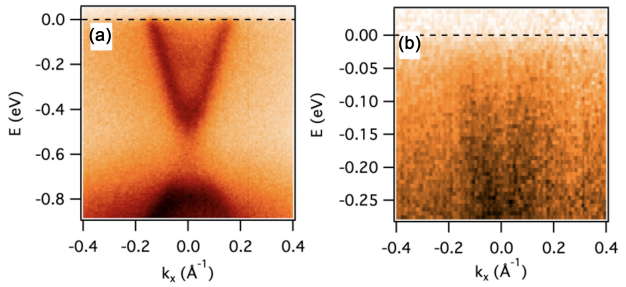

FIG. 11. Electron structures of Bi_2Se_3 films grown on BSCCO by ARPES measurements. (a) ARPES spectra of 1.5 QL and (b) 0.5 QL Bi_2Se_3 films[65]. Copyright ©2014, American Physical Society.

Due to the lack of direct evidence, the existence of the superconducting gap in the surface state is still controversial. For example, Yilmaz et al.[65] declares that

there is no evidence that superconducting gap exists in the topological surface of Bi_2Se_3. Figure 11 shows the ARPES measurements on the similar BSCCO/Bi_2Se_3 heterostructure, where there is a gap at Dirac point when the thickness of Bi_2Se_3 film is 1.5 QL. EDCs of Bi_2Se_3 films show that there is no clear gaps and coherence quasiparticle peaks in Bi_2Se_3 films. A short coherence length along c-axis in BSCCO is probably the main challenge to fabricate topological superconductor. Besides, the crystal quality and the sensitive interface also have to be seriously taken into account for the proximity effect based on BSCCO.

Proximity effect of high-temperature superconductor is a fascinating research field. The induced gap (about 10 meV) in BSCCO/Bi_2Se_3 heterostructure is an order of magnitude larger than in conventional superconductors (about 1 meV), which is quite suitable for detecting MZM. Moreover, the induced superconductivity will exist in a relatively high temperature, which is significant for practical applications. However, the short coherence length and the high instability of 2D BSCCO limit the fabrications and measurements of devices.

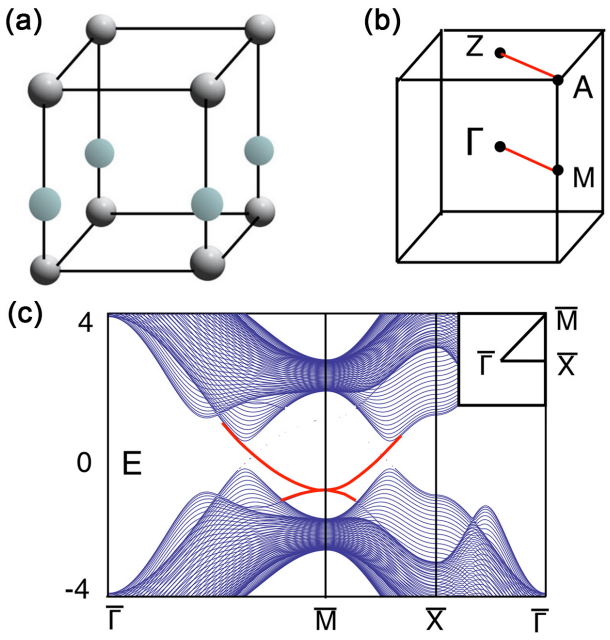

FIG. 12. (a) Tetragonal lattice with two atoms A and B along the c axis in the unit cell. (b) Four high symmetry points in the Brillouin zone. (c) Surface states with quadratic band touching exist on (001) surface[66]. Copyright ©2011, American Physical Society.

C. Hybrid junctions of topological insulators and superconducting Pb

1. Heterostructure of $Sn_{1-x}Pb_xTe$/Pb

Different from the time-reversal symmetry protected TI like Bi_2Se_3 and Bi_2Te_3, there is another class of TI called the topological crystalline insulators(TCIs), e.g., SnTe and $Sn_{1-x}Pb_x$(Se, Te), whose surface bands are protected by crystalline symmetry instead of time-reversal symmetry. Fu raised the concept of TCIs when studying the surfaces in highly symmetric systems[66]. By introducing a simple tight-binding model in a tetragonal crystal with C_4 symmetry, as shown in Figs. 12(a) and 12(b), Fu obtained a gapless surface state on the (001) crystal face, as shown in Fig. 12(c).

Soon after the theoretic prediction, TCIs were experimentally verified in SnTe-type IV-VI semiconductors, including isostructural PbTe and solid-solution system $Sn_{1-x}Pb_xTe$[67,68]. Due to the topological protection of lattice symmetries, TCIs are expected to form a new type of TSCs that multiple MZMs may bound to a single vortex[69,70]. Although several experiments have been made to induce bulk superconductivity in TCIs[71], there is still lack of direct evidence to demonstrate the existence of superconducting TCIs, except for the conventional full-gap STS spectra[72].

Recently, Jia et al.[55] investigated the superconductivity of $Sn_{1-x}Pb_xTe$/Pb heterostructures by STS spectra and found an unconventional peak-dip-hump gap feature, as shown in Fig. 13. The STS spectra show two sharp coherence peaks for both samples, indicating the induced superconductivity of $Sn_{1-x}Pb_xTe$. Besides, the superconducting proximity effect in this system is unexpectedly strong even at 4.2 K. Figure 13(b) shows the dI/dV spectrum taken on the Pb island, which is corresponding to the spectrum of a conventional superconductor. The broad shoulders at the outside sharp coherent peaks are due to the electron-phonon interaction. The black curve is the simulation according to the S-I-S model. Figure 13(c) shows the corresponding density of states (DOS) of Pb. The dI/dV spectrum of $Sn_{1-x}Pb_xTe$, shown in Fig. 13(d), is quite strange compared with that of Pb. Except for

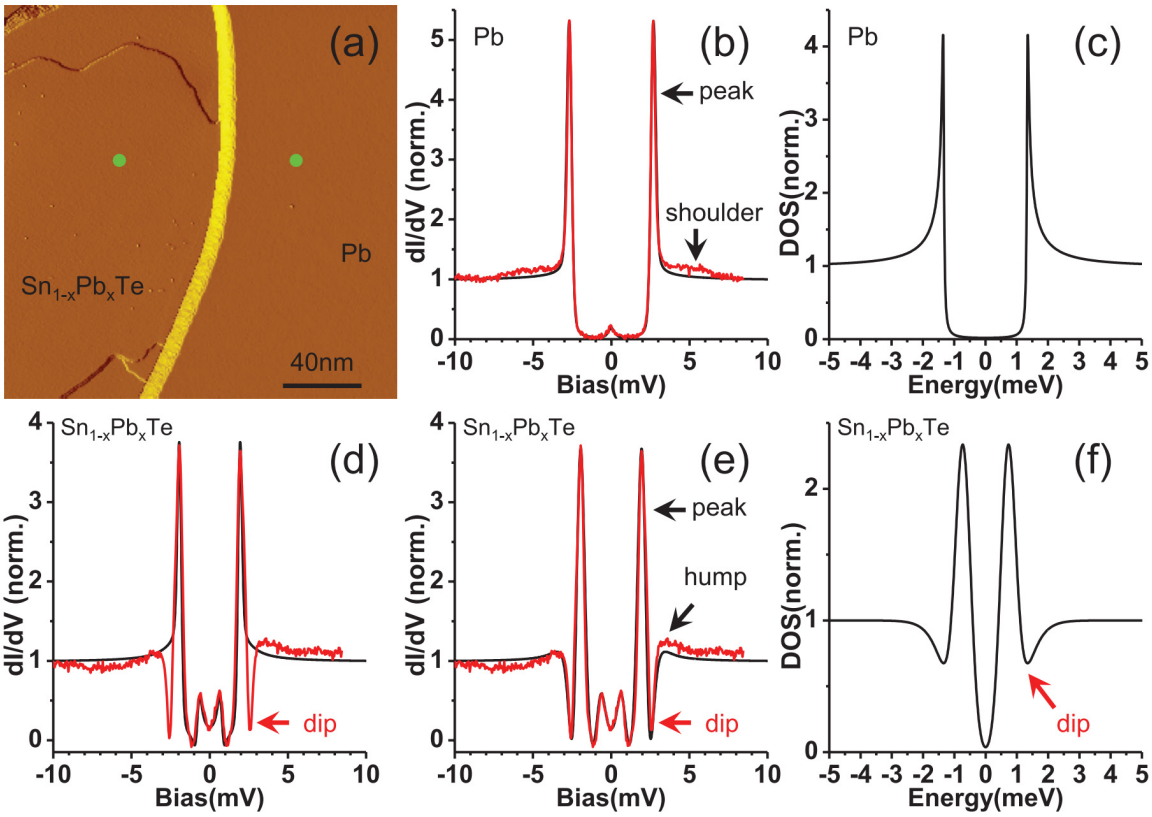

FIG. 13. Unconventional superconductivity of $Sn_{1-x}Pb_xTe$. (a) The STM topography of $Sn_{1-x}Pb_xTe$-Pb heterostructure. (b) The dI/dV spectrum of Pb at the position shown in (a). The black line is the simulated curve. (c) Corresponding sample DOS of Pb. (d) The dI/dV spectrum of $Sn_{1-x}Pb_xTe$ at the position shown in (a). The black line is the simulated curve with a BCS-like sample DOS. (e) The same dI/dV spectrum of $Sn_{1-x}Pb_xTe$ shown in (d). The black line is the simulated curve with a modified sample DOS. (f) Corresponding sample DOS of $Sn_{1-x}Pb_xTe$[55]. Copyright ©2019, Wiley.

the tunneling of thermal excitation induced small peaks around the zero bias voltage, there are two dips and two small humps outside the sharp peaks. The black curve in Fig. 13(d) is the simulated curve with a BCS-like sample DOS. Apparently, the simulated curve can fit the dI/dV spectrum well between the two sharp coherent peaks, but fails to fit the dip feature. By modifying the sample DOS, the simulated curve (black curve in Fig. 13(e)) can reproduce the peak and dip features very well. The corresponding sample DOS of $Sn_{1-x}Pb_xTe$ is shown in Fig. 13(f), which is obviously distinct from the BCS-like DOS of Pb in Fig. 13(c). All these results strongly support TSCs in $Sn_{1-x}Pb_xTe$/Pb heterostructrues induced by proximity effect.

The $Sn_{1-x}Pb_xTe$/Pb heterostructrues demonstrate a strong proximity effect. The induced superconductivity in $Sn_{1-x}Pb_xTe$ can still be observed up to 6.5 K, which even exceeds the maximum T_c (4.7 K) of In-doped $Sn_{1-x}Pb_xTe$[73]. Both the vertical and lateral heterostructures have a long coherence length which is above 200 nm. Furthermore, $Sn_{1-x}Pb_xTe$/Pb heterostructures fabricated by molecular beam epitaxy(MBE) can be atomically flat. Heterostructure is along the lateral direction or the vertical direction can be easily controlled by growth temperature. As a TCI, $Sn_{1-x}Pb_xTe$ is expected to form a new type of TSCs[74,75]. Unconventional superconductivity observed in SC/TCI heterostructrues need to be further explored.

2. Heterostructure of Pb/$TiBiSe_2$

We have discussed the realization of TSCs through inducing superconductivity in TI by superconducting proximity effect. Apparently, TSCs can also be obtained in SC by topological proximity effect, which

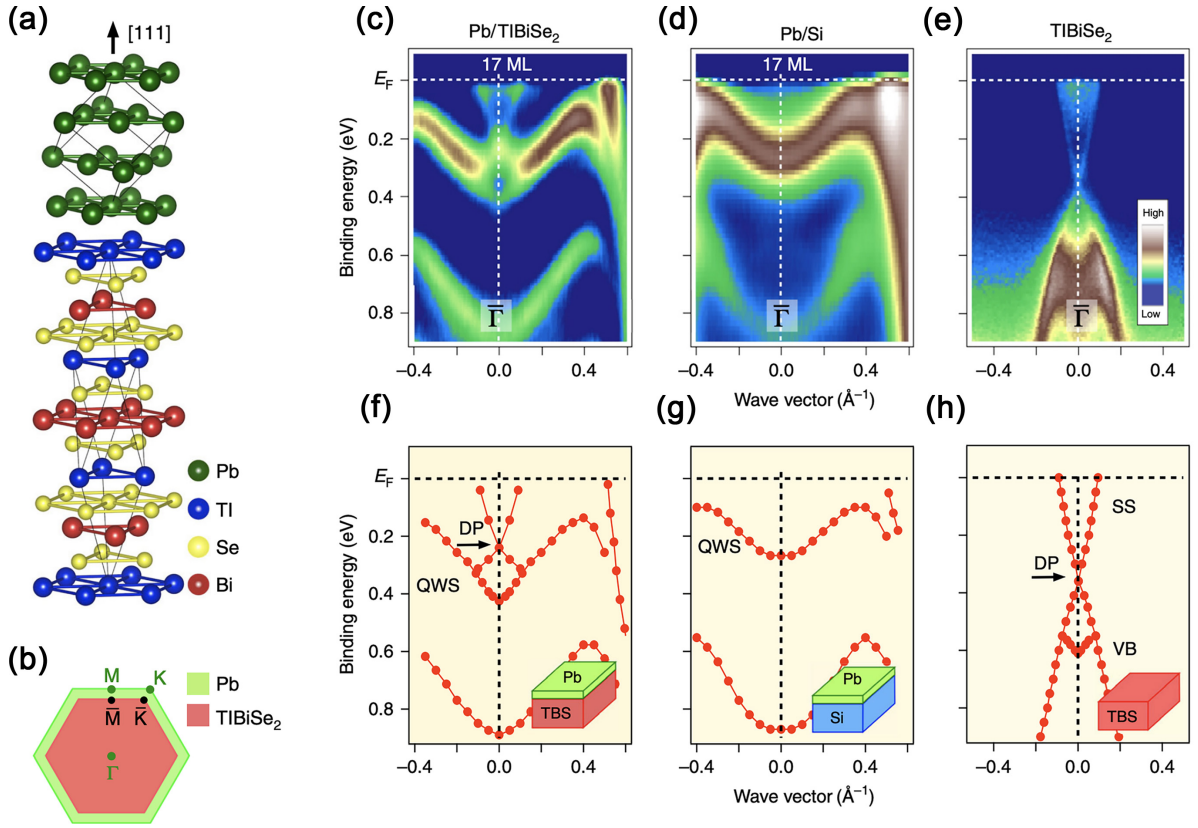

FIG. 14. Crystal and electronic structures of Pb(111) thin film on $TlBiSe_2$. (a) Schematic diagrams of Pt/$TlBiSe_2$ heterostructures. (b) Comparison of the Brillouin zone between Pb (green) and $TlBiSe_2$ (red). (c-e) ARPES-derived band structures near E_F around the $\bar{\Gamma}$ point for (c) 17ML-Pb/$TlBiSe_2$, (d) 17ML-Pb/Si(111), and (e) pristine $TlBiSe_2$, respectively. (f-h) Experimental band dispersions extracted from the peak positions of MDCs/EDCs for (c-e)[19]. Copyright ©2020, nature publishing group.

means the topological surface sates will migrate from TI to the adjacent SC.

Recently, Sato et al. proposed an approach to realize TSCs by topological proximity effect in Pb/$TiBiSe_2$ heterostructure[19]. They deposited Pb films on the $TiBiSe_2$ substrates by MBE. Figure 14(a) represents the schematic diagrams of crystal structures of Pb and $TiBiSe_2$. The in-plane lattice constant a of Pb and that of $TiBiSe_2$ are estimated to be 3.5 $\AA$ and 4.2 $\AA$ respectively by low-energy-electron-diffraction (LEED) and ARPES after deposition. Due to the mismatch of lattice constant, the Brillouin zone of Pb is slightly larger compared with $TiBiSe_2$, as shown in Fig. 14(b). The overall ARPES results reveal drastically changes of electronic structure after the deposition of Pd film on $TiBiSe_2$ (not shown in this paper). In brief, the valence band of $TiBiSe_2$ disappears while several **M**-shaped bands called quantum well states (QWSs) emerge. By the way, the thickness of Pb is estimated to be 17 MLs.

Figures 14(c-e) show ARPES-derived band structures near E_F around the $\bar{\Gamma}$ point with a higher resolution for 17ML-Pb/$TlBiSe_2$, 17ML-Pb/Si(111), and pristine $TlBiSe_2$, respectively. The 17ML-Pb/Si(111) is a control sample since the in-plane lattice constant of Pb/Si(111) is close to that of Pb/$TlBiSe_2$. Figures 14(f-h) represent the band dispersion extracted from the peak positions of EDC or MDC curves in Figs. 14(c-e). Obviously, there is an X-shaped band above the topmost QWSs band in Pb/$TlBiSe_2$ while it is absent in Pb/Si(111), which indicates that the band is not intrinsic for Pb film. Intuitively, the band is similar to the Dirac-cone surface states of pristine $TiBiSe_2$, as shown in Fig. 14(h). Moreover, the observed bands do not involve any trace of pristine $TiBiSe_2$ bands, e.g., the bulk valence band (labeled as VB in Fig. 14(h) lying below 0.4 eV in pristine $TiBiSe_2$, which rules out the possibility that the observed Dirac-cone-like band is due to the accidentally exposed surface sates of $TiBiSe_2$ through

holes of Pb thin film. Thus, the observed Dirac-cone-like bands indicate that the induced topological surface states in superconducting Pb originate from topological proximity effect.

Normally, the induced superconducting gap by proximity effect in the vertical SC/TI heterostructures is smaller than the intrinsic gap. The MZM is predicted to be localized in the vertex core of SC/TI interface[2]. These are ubiquitous obstacles for STM measurements. This work proposed a feasible method to realize TSC and directly detect MZMs on the top surface of SC grown on TI substrate by topological proximity effect, which is possible to realize TSCs in other SC/TI systems[76].

IV. TOPOLOGICAL INSULATOR-BASED JOSEPHSON JUNCTIONS

We have introduced several instances about proximity effect induced TSCs. Unlike conventional continuous phase transitions, topological phase transition does not break any symmetry, leading to the difficulties in revealing signatures of topological phases in TSCs. To date, the experimental evidence of nontrivial superconductivity mostly relies on the surface analysis, such as STM/STS or ARPES, as discussed in section III. In this section, we will discuss the transport properties of TSCs based on the S-TI-S Josephson junctions.

A. Josephson junction based on semiconductor quantum wells

For the 2D semiconductor quantum well system, the edge modes can be spin-polarized and cross-propagating. Pribiag et al. reported the superconductivity edge-mode of 2D quantum well system in the semiconducting InAs/GaSb quantum well[45], whose topological phase originates from type-II broken band alignment[77]. Moreover, they constructed a S-TI-S Josephson junction and demonstrated the bulk and edge dominated regions are gate-tunable by using superconductor quantum interference (SQI) techniques.

Figure 15(a) shows the cross-sectional view of the device layout. The contact separation (400 nm) is significant shorter than the edge mode decoherence length of superconducting aluminum (2∼4 μm)[78,79]. The superconducting material is composed of Ti(5 nm)/Al(150 nm), and the S-TI-S junction is sandwiched by a Ti/Au top gate and a n^+ GaAs substrate. With the top-gate voltage V_{tg} continually tuned from negative to positive, the Fermi level will move up from the valence band to the conduction band consecutively. Undoubtedly, the Fermi level will locate in the topological gap under certain V_{tg}.

When the Fermi level is tuned into the bulk band, the critical current density $J_c(x)$ is spatially homogeneous along the width at a perpendicular magnetic field B_z=0, as shown in the middle panel of Fig. 15(b), and the junction will act like a superconductor-normal-superconductor (SNS) junction. Since the Josephson supercurrent $I_c(B_z)$ is the Fourier transformation of the profile of J_c(x), the SQI pattern of a SNS junction yields a typical Fraunhofer pattern, as shown in the bottom of Fig. 15(b). In contrast, when the Fermi level is tuned into the topological gap, due to the edge-modes, the J_c(x) will mainly distribute in the edge, as shown in the middle panel of Fig. 15(c). As a consequence, the SQI pattern will form a well-known Φ_0-periodic superconducting quantum interference device (SQUID) pattern, which is revealed by the solid line in the bottom of Fig. 15(c). Especially when the edge-modes have helical characters, a $2\Phi_0$-periodic interference pattern is expected[9,10], as illustrated by the dashed lines in bottom of Fig. 15(c). Two dashed curves represent two different phases, which depend on the fermion parity of two edges[8].

In this Josephson junction based on InAs/ GaSb quantum wells, bulk-dominated and edge-dominated superconducting transport is highly tunable for electrostatic gating. An edge-dominated region which characterize the 2D topological phase arises only under conditions of high-bulk resistivity. This feature of InAs/ GaSb quantum wells makes it a promising platform to detect MZM.

B. Josephson junction based on HgTe

Different from InAs/GaSb, the TI phase in HgTe/HgCdTe originates from relativistic band-

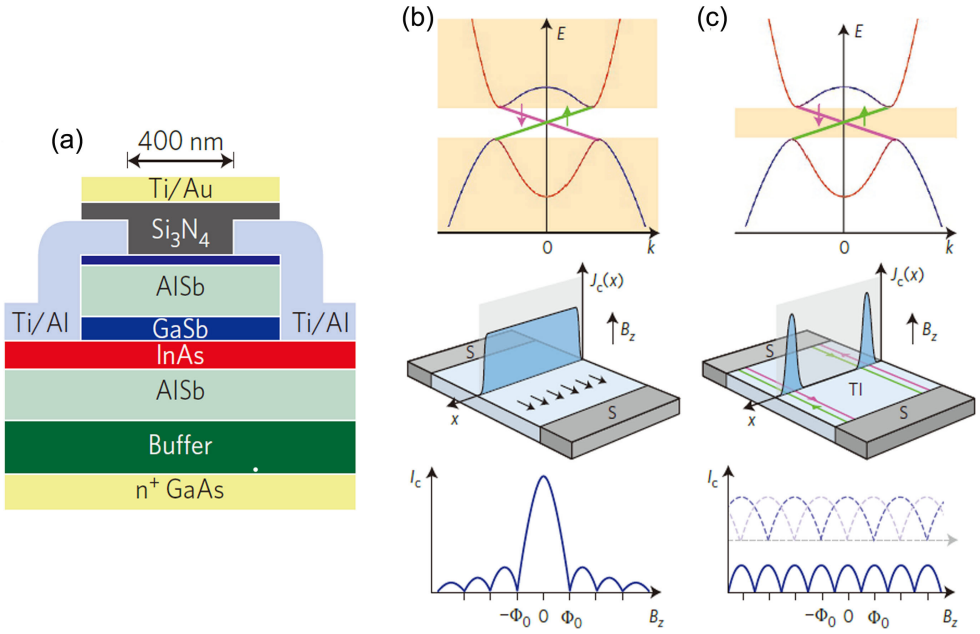

FIG. 15. (a) Cross-sectional view of device layout in the Al/InAs/Al junction. (b), (c) Top panel is the band structure of InAs/GaSb quantum wells. Linearly dispersive helical edge states exist between conduction band and valence band and arrows represent the spins of the states. Fermi level is in the bulk bands in (b) (orange rectangles), Fermi level is localized at the edge states in (c) (orange rectangles). Middle panel is the corresponding critical current density profile and bottom panel is the corresponding superconducting quantum interference pattern [45]. Copyright ©2015, nature publishing group.

bending [80]. As to the HgTe-based Josephson junctions, Ren et al. reported that the transition between topological phase and trivial phase can be tuned by an in-plane magnetic field and phase difference ϕ between two superconducting leads in a Al/HgTe/Al planar junction [46].

The Josephson junction composed of 2DEG HgTe and two superconducting leads Al is shown in Fig. 16(a). The ends of two Al leads are connected to form a flux loop. The phase difference are determined between two leads by applying an out-of-plane magnetic field B_z. Figure 16(b) shows the bound-state spectrum in a long clean junction. When the Zeeman energy is zero, Andreev states is two-fold degenerated (dashed line in Fig. 16(b)) and they will cross at the point $\phi = \pi$. When Zeeman energy is induced by an in-plane field B_x, double degenerate bound states are spin-split. Former cross point will also split into two cross points. At the range of ϕ between two cross points, topological phase will emerge. Figure 16(c) further depicts the relation between the Zeeman energy and the topological phase. As the Zeeman energy increases, the range of topological phase broadens from one point (ϕ=π) to the whole range of 2π and finally narrows to ϕ=π, which forms a periodic pattern until the superconductivity is totally suppressed. Ideal topological phase is a diamond shape(dashed lines). When the normal reflection is taken into consideration, the phase accumulated by quasiparticles transverse from x direction will make the phase boundary deviate from the ideal shape.

Figures 16(d)-(f) show the periodic modulation of differential conductance by $\Delta\phi$ and dc bias voltages under different B_xs. When the Zeeman energy is zero, the differential conductance curve is similar to a conventional superconductor. A couple of coherence peaks is about 120 μV, as shown in Fig. 16(g). At four representative phase difference, all the differential conductance curves have a valley shape near zero bias. When B_x= 0.7 T, the shape of the differential conductance curve at ϕ=π changes, depicted in Fig. 16(h). The valley shape near zero bias involves into a little peak, differential conductance curves at other three phases remain unchanged. It indicates that B_x= 0.7 T is near topological transition boundary for ϕ=π. When B_x= 1 T, the differential conductance curve at ϕ=π has a

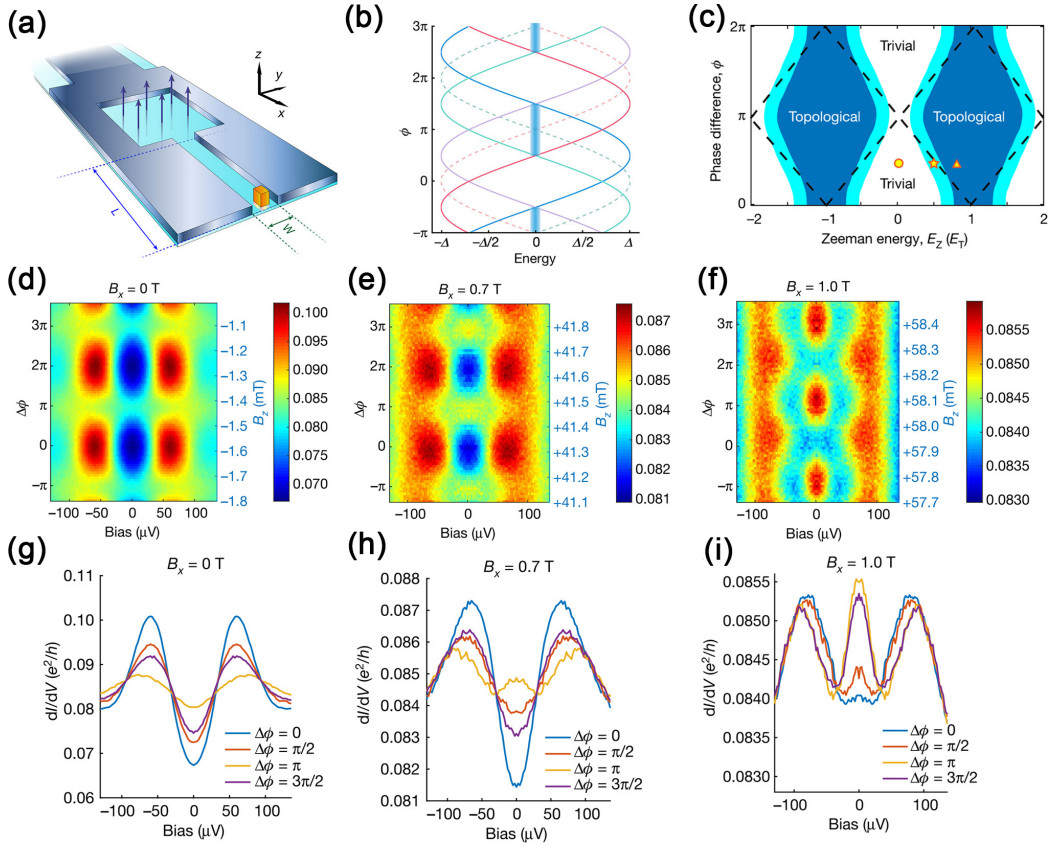

FIG. 16. Topological transition in Al/HgTe/Al Josephson junction. (a) Schematic image of the Josephson junction which is composed of HgTe 2DEG (cyan) and two superconducting leads Al (steel blue). The length and width of junction are L and W, respectively. The ends of two superconducting leads are connected to form a flux loop. The tunnel probe tip (gold) is on top of HgTe 2DEG, but is separated from it by a HgCdTe film. (b) Bound-state spectrum for k_x=0. The energy is in unit of Δ (induced superconducting gap). Dashed lines represent bound states when Zeeman energy is zero, while solid lines represent nonzero Zeeman energy bound states. (c) Phase diagram in ϕ-E_z space. ϕ is the phase difference between two superconducting leads and E_z is the Zeeman energy. Blue shaded regions represent topological phase. The deviation of topological phase regions from the diamond shape (dashed line) to the light blue ribbon shape is caused by the normal reflection at the interface. (d)-(f) Differential conductance color maps as the functions of dc voltage bias and phase difference $\Delta\phi$ with B_x=0 T, 0.7 T and 1.0 T, respectively. The conductance is in unit of e^2/h. (g)-(i) Line cuts of (d)-(f) at $\Delta\phi$=0, $\pi/2$, π and $3\pi/2$[46]. Copyright ©2019, nature publishing group.

sharp zero-bias peak. Zero-bias peak persists over a wide range of ϕ, which indicates a wide range of ϕ in topological phase. The report extracted zero-bias curvature in different ϕ and Zeeman energy to plot a phase diagram of the device (not shown in this paper). The phase diagram is similar to Fig. 16(c). When B_x is low , differential conductance curve at ϕ=π does not have the a zero-bias peak which indicates a trivial phase. It's attributed to the disturbance of normal reflection in superconducting-normal interface.

A general method to realize the transition from trivial phase to topological phase is to tune the Fermi level[45,48]. However, in the HgTe/HgCdTe based Josephson junctions, the topological transition could be controlled by in-plane and out-of-plane magnetic fields, which is more convenient and practical. Zero-bias peaks characterized topological phase can be tuned to be sharp and persist in a wide range of phase, which paves the way for manipulating MZMs.

C. Josephson junction based on WTe_2

WTe_2 is a type-II Weyl semimetal. In bulk WTe_2, the topological surface state is believed to emerge in the form of Fermi arcs, connecting the projected Weyl points in momentum space[81]. Recently, it is proposed that bulk WTe_2 in its Td structure (non-centrosymmetric and orthorhombic) is a higher-order

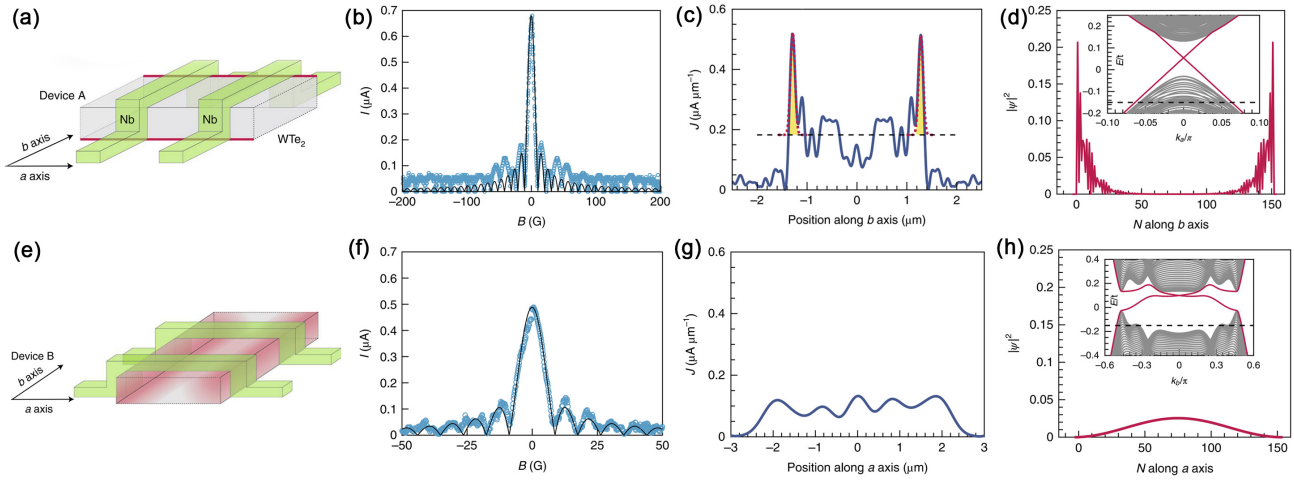

FIG. 17. Superconducting interference pattern in $Nb/WTe_2/Nb$ Josephson junction and extracted current profiles. Schematic images of Josephson junctions based on WTe_2 with the current propagating (a) along a axis in device A and (e) along b axis in device B. Thick red lines in (a) represent well-localized hinge states along the a axis. The region shaded red in (e) represents delocalized hinge states along the b axis. The SQI patterns corresponding to (b) device A and (f) device B, respectively. Black lines represent the standard single-slit Fraunhofer patterns. The extracted critical current density spatial distribution for (c) device A and (g) device B, respectively. Calculated wave functions of hinge states (d) along a axis and along (h) b axis, respectively. The Insets in (d) and (h) are the calculated energy bands along a axis and along b axis, respectively. Red lines represent the edge states and grey lines represent the bulk states, black dashed line represents the Fermi level [47]. Copyright ©2020, nature publishing group.

topological insulator (HOTI) and has topologically protected helical hinge states [82]. A big difference from the conventional TI is that WTe_2 is bulk-conducted. Therefore, it is a challenge to differentiate the boundary states from bulk states by electrical transport measurements.

Choi et al. reported anisotropic hinge states in WTe_2 by electrical transport measurements based on the Josephson coupling between WTe_2 and superconductor Nb [47]. Figures. 17(a) and 17(e) are schematic images of Josephson junctions with the current propagating along a axis and b axis of WTe_2, respectively. Figures 17(b) and 17(f) show the superconducting quantum interference(SQI) patterns of both geometries. The SQI pattern of device B is in good agreement with the standard Fraunhofer pattern, which is shown as black lines in Figs. 17(b) and 17(f). On the contrary, the SQI pattern of device A does not obey the Fraunhofer pattern and the oscillation of critical current exists even under fairly high magnetic field. The SQI pattern is closely related to the distribution of current density, which is shown in Figs. 17(c) and 17(g). There are two peaks of critical current density at two edges in device A, which is apparently the signature of edge states. The edge states are depicted by red line along a axis in Fig. 17(a). however, the critical current density is uniformly distributed in device B, as shown in red region of Fig. 17(e). The highly anisotropic hinge states in experiment is consistent with the result of theoretical calculation shown in Figs. 17(d) and 17(h). The corresponding SQI pattern is a standard Fraunhofer pattern. To differentiate between the (1D) hinge-state scenario and the (2D) Fermi arc surface-state scenario, a control experiment is performed that using insulating Al_2O_3 to change the critical current distribution. (not shown in this paper). Experimental measurement results are in good agreement with the (1D) hinge-state scenario.

The coupling between superconductors and Weyl semimetals generates a lot of interesting physical phenomena. An obvious point is that the strength of coupling with the superconductor is selective for boundary states and bulk states. Andreev reflections in bulk states are suppressed due to conservation of chirality [83]. However, the coupling between topological boundary states and superconductivity makes Weyl semimetals, especially HOTI systems, an ideal platform for TSC research [84–87]. The anisotropic 1D hinge states observed in bulk WTe_2 are naturally 1D

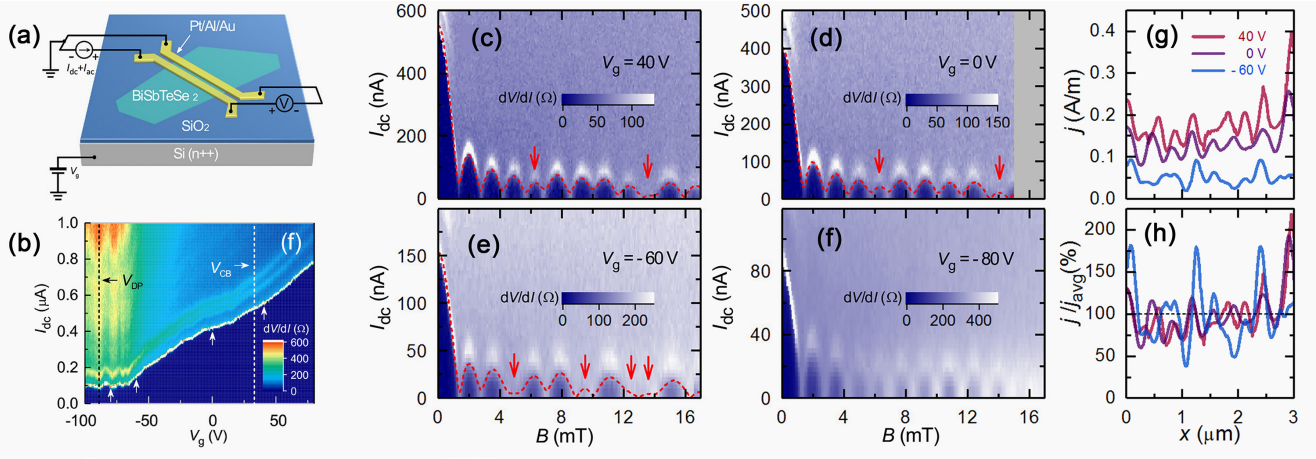

FIG. 18. Anomalous Fraunhofer patterns in Al/ $BiSbTeSe_2$/Al Josephson junction. (a) Schematic image of Josephson junction based on $BiSbTeSe_2$. (b) Differential resistance as a function of gate voltage and dc current. Black dashed line represents the Dirac point and white dashed line represents conduction band. (c)-(f), SQI patterns at fixed gated voltage 40 V, 0 V, −60 V and −80 V, respectively. The voltage is labeled by white arrows in figure (b). The temperature of measurement is 8 mK. Red dashed lines are the fits to experimental data using the maximum entropy method in a Monte Carlo algorithm. (g) Critical current density distribution $j(x)$. (h) The normalized critical current density distribution $j(x)/j_{avg}$ is the result of fitting indicated by red dashed lines in (c)-(e)[48]. Copyright ©2018, American Chemical Society.

topological-protected superconducting wires. Properties of hinge states such as the interplay with the magnetic order need to be further explored.

D. Josephson junction based on $BiSbTeSe_2$

MZMs are predicted to exist in Josephson junction based on 3D TI. Fraunhofer patterns in such topological Josephson junctions sometimes present anomalous features while the quantum mechanism is hard to understand. Gahatak et al. reported an anomalous Fraunhofer pattern in Josephson junction based on $BiSbTeSe_2$ and attributed it to the inhomogeneous critical current distribution[48].

$BiSbTeSe_2$ is a bulk-insulating 3D TIs, which is advantageous to investigate topological edge states[88]. Figure 18(a) is the device structure of Josephson junction. $BiSbTeSe_2$ is Josephson coupled with superconductor Al leads. The distance between two leads is 70 nm and the width is 2.9 μm. Whether the "eI_cR_n-to-Δ ratio" or the Multiple Andreev reflections results indicates the high transparency of the junction. Figure 18(b) shows the color map of the differential resistance versus dc current with different gating voltage. The white solid line represents the critical current with different gating voltage, which decreases when the Fermi level is tuned from conduction band to the Dirac point and even keeps nonzero at the Dirac point, indicating the realization of the proximity-induced surface superconductivity during the whole range of gating voltage. The corresponding gating voltage of conduction band (V_{CB}) and the Dirac point (V_{DP}) are labeled as white and black dashed lines in Fig. 18(b).

Figures 18(c)-(f) depict the anomalous Fraunhofer patterns at V_g= 40 V, 0 V, −60 V and −80 V, which are labeled as while arrows in Fig. 18(b). There are several lobes disappear in these Fraunhofer patterns, which could be generated by two mechanisms: One is the nonsinusoidal phase relation, which is closely connected with the 4π-periodic current-phase relation of MZMs[89]. In this situation, odd-number lobes will be suppressed in Fraunhofer patterns, which cannot interpret the particular patterns in this experiment[90]. The second mechanism is due to the inhomogeneous critical current distribution. Figures 18(g) and 18(h) are the inhomogeneous critical current distribution of the junction obtained by fitting. Fluctuation of the junction length $L(x)$ due to roughness of superconducting lead Al and position-dependent transparency of SC/TI interface may cause the inhomogeneous distribution of supercurrent.

This report successfully fabricated a highly gate-

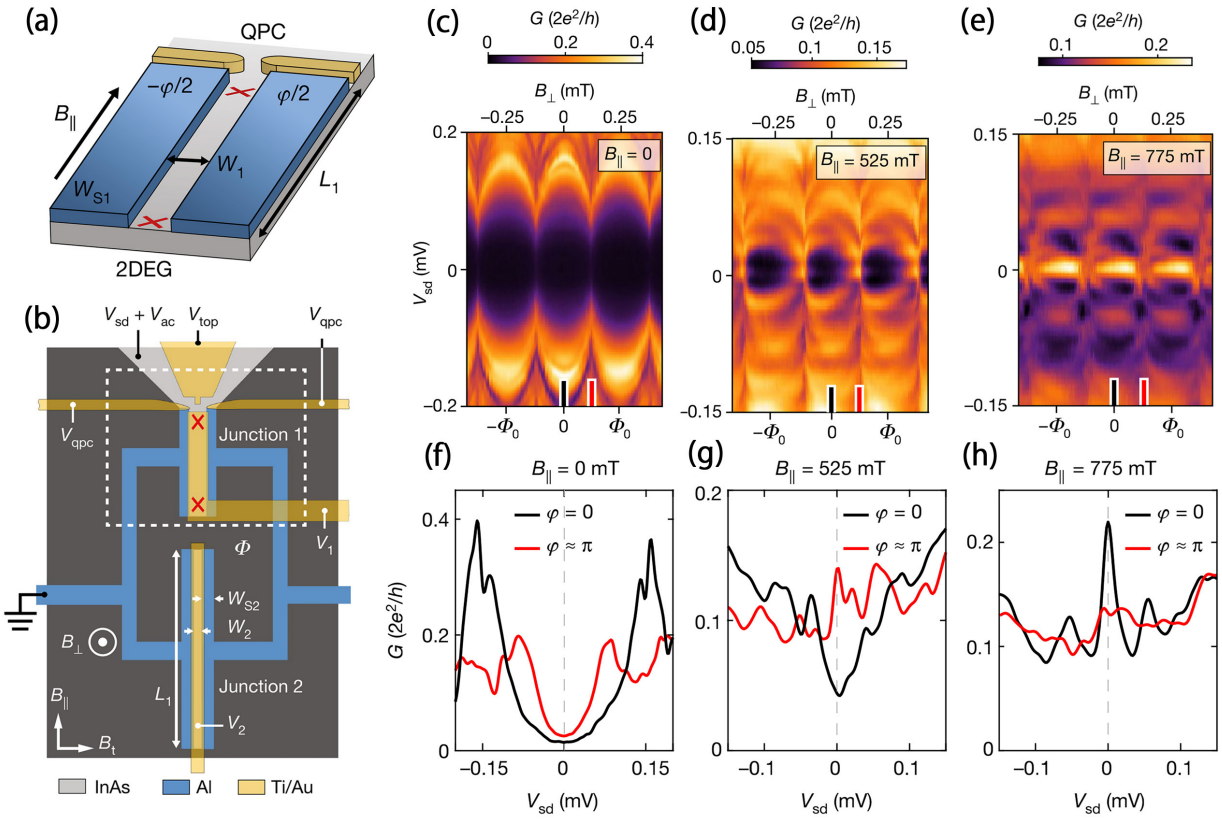

FIG. 19. Topological superconductivity tuned by Zeeman energy in Al/InAs/Al Josephson junction. (a) Schematic image of a planar Josephson junction. Planar Josephson junction contains a 2DEG and two superconducting stripes. (b) Schematic image of the SQUID composed of two Al/InAs/Al Josephson junctions. V_{QPC} is used to measure the local DOS. V_1 and V_2 are used to tune Fermi energy of JJ_1 and JJ_2, respectively. (c-e) Differential conductance as a function of magnetic flux in different Zeeman energy. Magnetic flux is tuned by $B_\perp$ and Zeeman energy is tuned by $B_\parallel$. (f-h) Line-cuts of differential conductance in figure (c-e). Black lines represent differential conductance spectra when phase ϕ=0 and red lines represents differential conductance spectra when phase ϕ=π [49]. Copyright ©2019, nature publishing group.

tuned planar Josephson junction and quantitatively analyzed the anomalous Fraunhofer patterns using maximum entropy method in a Monte Carlo algorithm [91]. This method removes the constraint of the standard Dynes-Fulton-type analysis and is able to identify any form of inhomogeneous supercurrent distribution [92]. The techniques applied in this experiment are helpful for the detection of MZMs in topological Josephson junctions.

E. Topological insulator based SQUID

Since the planar Josephson junction is a promising platform to create and manipulate MZMs, Fornieri et al. investigated the phase dependent topological superconductivity in Al/InAs heterostructures by the method of SQUID [49]. In this heterostructure, 2DEG InAs is a suitable material to fabricate S-TI-S junction due to the high electron mobility and strong spin-orbit interaction [93], while aluminum has a long electronic coherence length below T_c which is suitable for Josephson junction fabrication. The superconductor-semiconductor interface between InAs and epitaxially covered aluminum is measured to be high transparency [94], and the induced superconducting gap in InAs was reported to be closed to the intrinsic superconducting gap of aluminum [95].

The schematic of the planar Josephson junction consisting of two superconductor (Al) stripes and a 2DEG (InAs) layer is shown in Fig. 19(a). The phase dependence of topological superconductivity is measured by the laterally coupled quantum point contacts (QPC) when embedding the junction into a dc SQUID,

as shown in Fig. 19(b). The top junction is labeled as Junction 1 (JJ1), and the bottle one is labeled as Junction 2 (JJ2). A dc voltage combined with a small ac voltage is added into the QPC to measure the differential conductance (G) of JJ1. The top gate is used to define a sharp tunnel barrier when the top gate voltage is near zero[49]. The SQUID is asymmetry due to different sizes of JJ1 and JJ2.

The oscillations of G as a function of magnetic flux Φ_0, which is tuned by $B_\perp$, under different dc voltages ($V_{\rm sd}$) are shown in Figs. 19(c-e). The in-plane magnetic fields $B_\parallel$s are 0 mT, 525 mT and 775 mT respectively for these three patterns. Figures 19(f-h) represent G versus $\rm V_{sd}$ curves at $\varphi = 0$ and $\varphi = \pi$ under different $\rm B_\parallel$s, which are labeled as black and red lines in Figs. 19(c-e). Obviously, The zero-bias conductance is nearly the same when magnetic field $B_\parallel$=0 mT, as shown in Fig. 19(f). The electric transportation is phase-coherent which is resulted from the Andreev reflection at the interface. The minimum of superconducting gap in JJ1 is unable to be tuned to zero due to the finite sized width. But a finite sized width is necessary for Josephson junctions to keep a large enough induced gap when magnetic field is 1 T. Zeeman energy induced by $B_\parallel$ determines the emergence of zero-bias conductance peak (ZBP). When $B_\parallel$ increases continually, discrete Andreev bound states move to zero energy. When $B_\parallel$ is 525 mT, the ZBP emerges at $\varphi = \pi$ and disappears at $\varphi = 0$, as shown in Fig. 19(g). The ZBP will extend from $\varphi = \pi$ in phase space. When $B_\parallel$ is increased to 775 mT, as shown in Fig. 19(h), ZBP emerges in $\varphi = \pi$ and exists at the whole range of phase φ. ZBCP of $\varphi = 0$ will last when in-plane magnetic field $B_\parallel$ is large enough, indicating that MZMs will emerge at full range of the JJ1 and MZMs will last at full range of phase.

In-plane magnetic field $B_\parallel$, phase difference φ and chemical potential are applied to tune topological phase in the SQUID. In the experiment, ZBP characterizing topological phase is rather sensitive to the change of phase difference φ. The range of φ that ZBP emerges is dependent on chemical potential and in-plane field. The dependence of ZBP is qualitative in agreement with theoretical calculation of a finite-size topological Josephson junction, it can be well understood as the behavior of Majorana wavefunction. The influence of chemical potential dependents on the geometry of junction. Consequently, if the influence of chemical potential can be suppressed, the design of topologically protected quantum device will be greatly simplified[96,97]. This is one of the main motivation for future materials and design improvements[98,99].

V. SUMMARY

In this review, we give an overview of the proximity effect induced topological superconductivity in TI/SC heterostructures. The topological superconductivity is a promising way to avoid the problem of maintaining coherence in quantum computation, and provides an ideal route for fault-tolerant quantum computation and superconducting spintronics. The most practical way to induce topological superconductivity is through proximity effect, which is dominated by the properties of the TIs and the corresponding interface between the TIs and the s-wave SCs. Here, we introduce the general backgrounds of TIs, the proximity effect of superconductivity, the TSCs, the MZMs, and the theoretical Fu-Kane model. Besides, we review the recent experimental progress on TSCs and MZMs in both hybrid structure devices and JJs. For the hybrid structure devices, we introduce the 3D TI (Bi_2Se_3) on s-wave SC ($NbSe_2$) and d-wave SC ($Bi_2Sr_2CaCu_2O_{8+\delta}$), TCI ($Sn_{1-x}Pb_xTe$) on Pb, 2D TI ($WTe_2$) on s-wave SC ($NbSe_2$), and the topological insulating proximity effect of $TiBiSe_2$ on Pb. For the JJs, we introduce the TI based Josephson junctions based on Fu-Kane system, and the superconducting quantum interference device by TI based Josephson junctions.

ACKNOWLEDGMENTS

This research was supported in part by the National Natural Science Foundation of China (Nos. 61771234, 12004251), National Key Projects for Research and Development of China (No. 2017YFB0503302), the Natural Science Foundation of Shanghai (No. 20ZR1436100), the Science and Technology Commission of Shanghai Municipality, the startup

funding from ShanghaiTech University, and Beijing National Laboratory for Condensed Matter Physics.

REFERENCES

[1] Nayak C, Simon S H, Stern A, et al. *Rev. Mod. Phys.*, 2008, **80**(3): 1083

[2] Fu L, Kane C L. *Phys. Rev. Lett.*, 2008, **100**: 096407

[3] Alicea J. *Rep. Prog. Phys.*, 2012, **75**(7): 076501

[4] Tewari S, Das Sarma S, Nayak C, et al. *Phys. Rev. Lett.*, 2007, **98**(1): 010506

[5] Moore G, Read N. *Nucl. Phys. B*, 1991, **360**(2-3): 362

[6] Kitaev A Y. *Ann. Phys.*, 2003, **303**(1): 2

[7] Wilczek F. *Nat. Phys.*, 2009, **5**(9): 614

[8] Lee S P, Michaeli K, Alicea J, et al. *Phys. Rev. Lett.*, 2014, **113**(19): 197001

[9] Qi X L, Zhang S C. *Rev. Mod. Phys.*, 2011, **83**(4): 1057

[10] Hasan M Z, Kane C L. *Rev. Mod. Phys*, 2010, **82**(4): 3045

[11] Mackenzie A P, Maeno Y. *Rev. Mod. Phys.*, 2003, **75**: 657

[12] Kallin C. *Rep. Prog. Phys.*, 2012, **75**(4): 042501

[13] Pustogow A, Luo Y, Chronister A, et al. *Nature*, 2019, **574**(7776): 72

[14] Sasaki S, Kriener M, Segawa K, et al. *Phys. Rev. Lett.*, 2011, **107**: 217001

[15] Liu Z, Yao X, Shao J, et al. *J. Am. Chem. Soc*, 2015, **137**(33): 10512

[16] Asaba T, Lawson B J, Tinsman C, et al. *Phys. Rev. X*, 2017, **7**: 011009

[17] Wang D, Kong L, Fan P, et al. *Science*, 2018, **362**(6412): 333

[18] Wang M X, Liu C, Xu J P, et al. *Science*, 2012, **336**(6077): 52

[19] Trang C X, Shimamura N, Nakayama K, et al. *Nat. Commun.*, 2020, **11**(1): 159

[20] Lpke F, Waters D, de la Barrera S C, et al. *Nat. Phys.*, 2020, **16**(5): 526

[21] Klitzing K V, Dorda G, Pepper M. *Phys. Rev. Lett.*, 1980, **45**(6): 494

[22] Tsui D C, Stormer H L, Gossard A C. *Phys. Rev. Lett.*, 1982, **48**(22): 1559

[23] Wen X G. *Adv. Phys.*, 1995, **44**(5): 405

[24] Thouless D J, Kohmoto M, Nightingale M P, et al. *Phys. Rev. Lett.*, 1982, **49**(6): 405

[25] Kane C L, Mele E J. *Phys. Rev. Lett.*, 2005, **95**(22): 226801

[26] Bernevig B A, Hughes T L, Zhang S C. *Science*, 2006, **314**(5806): 1757

[27] Kane C L, Mele E J. *Phys. Rev. Lett.*, 2005, **95**(14): 146802

[28] Chang C Z, Zhang J S, Feng X, et al. *Science*, 2013, **340**(6129): 167

[29] Caroli C, de Gennes P G, Matricon J. *Phys. Lett.*, 1964, **9**: 307

[30] Volovik G E. *JETP Lett.*, 1999, **70**: 609

[31] Read N, Green D. *Phys. Rev. B*, 2000, **61**(15): 10267

[32] Nelson K D, Mao Z Q, Maeno Y, et al. *Science*, 2004, **306**(5699): 1151

[33] Mackenzie A P, Maeno Y. *Rev. Mod. Phys.*, 2003, **75**: 657

[34] Sauls J A. *Adv. Phys.*, 1994, **43**(1): 113

[35] Wang J, Zhang S C. *Nat. Mater.*, 2017, **16**(11): 1062

[36] Majorana E. *Nuovo Cimento*, 1937, **14**: 171

[37] He Q L, Pan L, Stern A L, et al. *Science*, 2017, **357**(6348): 294

[38] Elliott S R, Franz M. *Rev. Mod. Phys.*, 2015, **87**(1): 137

[39] Greiter M, Wen X G, Wilczek F. *Nucl. Phys. B*, 1992, **374**(3): 567

[40] Gurarie V, Radzihovsky L, Andreev A V. *Phys. Rev. Lett.*, 2005, **94**(23): 230403

[41] Sato M, Fujimoto S. *Phys. Rev. B*, 2009, **79**(9): 094504

[42] Sau J D, Lutchyn R M, Tewari S, et al. *Phys. Rev. Lett.*, 2010, **104**(4): 040502

[43] Nielssen H, Ninomiya N. Phys. Lett. B, 1983. 130: 389

[44] Volkov A F, Magnee P H C, Vanwees B J, et al. *Physica C*, 1995, **242**(3-4): 261

[45] Pribiag V S, Beukman A J A, Qu F, et al. *Nat. Nanotechnol.*, 2015, **10**(7): 593

[46] Ren H, Pientka F, Hart S, et al. *Nature*, 2019, **569**(7754): 93

[47] Choi Y B, Xie Y, Chen C Z, et al. *Nat. Mater.*, 2020, **19**(9): 974

[48] Ghatak S, Breunig O, Yang F, et al. *Nano Lett.*, 2018, **18**(8): 5124

[49] Fornieri A, Whiticar A M, Setiawan F, et al. *Nature*, 2019, **569**(7754): 89

[50] Wang M X, Liu C, Xu J P, et al. *Science*, 2012, **336**(6077): 52

[51] Teo J C Y, Kane C L. *Phys. Rev. Lett.*, 2010, **104**: 046401

[52] Sun H H, Zhang K W, Hu L H, et al. *Phys. Rev. Lett.*, 2016, **116**(25): 257003

[53] He J J, Ng T K, Lee P A, et al. *Phys. Rev. Lett.*, 2014, **112**(3): 037001

[54] Wang E, Ding H, Fedorov A V, et al. *Nat. Phys.*, 2013, **9**(10): 621

[55] Yang H, Li Y Y, Liu T T, et al. *Adv. Mater.*, 2019, **31**(52): 1905582

[56] Haim A, Berg E, von Oppen F, et al. *Phys. Rev. Lett.*, 2015, **114**(16): 166406
[57] Kawakami T, Hu X. *Phys. Rev. Lett.*, 2015, **115**(17): 177001
[58] Qian X F, Liu J W, Fu L, et al. *Science*, 2014, **346**(6215): 1344
[59] Tang S J, Zhang C F, Wong D, et al. *Nat. Phys.*, 2017, **13**(7): 683
[60] Fei Z Y, Palomaki T, Wu S F, et al. *Nat. Phys.*, 2017, **13**(7): 677
[61] Wu S F, Fatemi V, Gibson Q D, et al. *Science*, 2018, 359(6371): 76
[62] Fatemi V, Wu S F, Cao Y, et al. *Science*, 2018, **362**(6417): 926
[63] Sajadi E, Palomaki T, Fei Z Y, et al. *Science*, 2018, **362**(6417): 922
[64] Zareapour P, Hayat A, Zhao S Y F, et al. *Nat. Commun.*, 2012. **3**(1): 1056
[65] Yilmaz T, Pletikosić I, Weber A P, et al. *Phys. Rev. Lett.*, 2014, **113**: 067003
[66] Fu L. *Phys. Rev. Lett.*, 2011, **106**(10): 106802
[67] Hsieh T H, Lin H, Liu J, et al. *Nat. Commun.*, 2012, **3**: 982
[68] Tanaka Y, Ren Z, Sato T, et al. *Nat. Phys.*, 2012, **8**(11): 800
[69] Fang C, Gilbert M J, Bernevig B A. *Phys. Rev. Lett.*, 2014, **112**(10): 106401
[70] Liu X J, He J J, Law K T. *Phys. Rev. B*, 2014, **90**(23): 235141
[71] Sasaki S, Ren Z, Taskin A A, et al. *Phys. Rev. Lett.*, 2012, **109**(21): 217004
[72] Du G, Du Z, Fang D, et al. *Phys. Rev. B*, 2015, **92**: 020512
[73] Zhong R D, Schneeloch J A, Liu T S, et al. *Phys. Rev. B*, 2014, **90**(2): 020505(R)
[74] Fang C, Gilbert M J, Bernevig B A. *Phys. Rev. Lett.*, 2014, **112**(4): 046801
[75] Liu X J, He J J, Law K T. *Phys. Rev. B*, 2014, **90**: 235141
[76] Shoman T, Takayama A, Sato T, et al. *Nat. Commun.*, 2015, **6**: 6547
[77] Liu C, Hughes T L, Qi X L, et al. *Phys. Rev. Lett.*, 2008, **100**: 236601
[78] Du L J, Knez I, Sullivan G, et al. *Phys. Rev. Lett.*, 2015, **114**(9): 096802
[79] Knez I, Du R R, Sullivan G. *Phys. Rev. Lett.*, 2011, **107**(13): 136603
[80] Hart S, Ren H, Wagner T, et al. *Nat. Phys.*, 2014, **10**(9): 638
[81] Soluyanov A A, Gresch D, Wang Z, et al. *Nature*, 2015, **527**(7579): 495
[82] Wang Z, Wieder B J, Li J, et al. *Phys. Rev. Lett.*, 2019, **123**(18): 186401
[83] Bovenzi N, Breitkreiz M, Baireuther P, et al. *Phys. Rev. B*, 2017, **96**(3): 035437
[84] Khanna U, Kundu A, Pradhan S, et al. *Phys. Rev. B*, 2014, **90**(19): 195430
[85] Faraei Z, Jafari S A. *Phys. Rev. B*, 2019, **100**(3): 035447
[86] Bruno F Y, Tamai A, Wu Q S, et al. *Phys. Rev. B*, 2016, **94**(12): 121112(R)
[87] Zhang W H, Wu Q S, Zhang L Y, et al. *Phys. Rev. B*, 2017, **96**(16): 165125
[88] Ren Z, Taskin A A, Sasaki S, et al. *Phys. Rev. B*, 2011, **84**(16): 165311
[89] Potter A C, Fu L. *Phys. Rev. B*, 2013, **88**(12): 115137
[90] Baxevanis B, Ostroukh V P, Beenakker C W J. *Phys. Rev. B*, 2015, **91**(4): 041409(R)
[91] Jaynes E T. *Phys. Rev.*, 1957, **106**: 620
[92] Dynes R C, Fulton T A. *Phys. Rev. B*, 1971, **3**(9): 3015
[93] Shabani J, Kjaergaard M, Suominen H J, et al. *Phys. Rev. B*, 2016, **93**: 155402
[94] Krogstrup P, Ziino N L B, Chang W, et al. *Nat. Mater.*, 2015, **14**(4): 400
[95] Kjaergaard M, Suominen H J, Nowak M P, et al. *Phys. Rev. Appl.*, 2017, **7**: 034029
[96] Hell M, Leijnse M, Flensberg K. *Phys. Rev. Lett.*, 2017, **118**(10): 107701
[97] Pientka F, Keselman A, Berg E, et al. *Phys. Rev. X*, 2017, **7**(2): 021032
[98] Drachmann A C, Suominen H J, Kjaergaard M, et al. *Nano Lett.*, 2017. **17**(2): 1200
[99] Delfanazari K, Puddy R K, Ma P, et al. *Adv. Mater.*, 2017, 29(37): 1701836

拓扑绝缘体/超导体异质结中的近邻效应

贺家电 [1,2]，丁逸凡 [1,2]，滕博伦 [1,2]，董　鹏 [1,2]，李逸飞 [1,2]，张忆文 [1,2]，吴越珅 [1,2]，王靖珲 [1,2]，周　翔 [1,2]，王　志 [3]，李　军 [1,2]

1. 物质科学与技术学院，上海科技大学，上海，200031，中国
2. 拓扑物理实验室，上海科技大学，上海，200031，中国
3. 物理学院，中山大学，广州，510275，中国

摘要：拓扑超导体自身具有对量子退相干天然的免疫性以及可编织性，这使得它在现代量子计算领域中受到了越来越多的重视，并且成为了下一代计算技术中最有希望的候选者之一。由于拓扑超导态在固有拓扑超导体中相当罕见，因此，当前大部分实验上的工作主要集中在由 s 波超导体与拓扑绝缘体之间通过近邻效应所诱导的拓扑超导体上。本论文中，我们回顾了基于拓扑绝缘体/超导体异质结的拓扑超导体的研究进展。在理论上，Fu 和 Kane 提出，通过近邻效应将 s 波超导体的能隙引入到拓扑绝缘体，可以诱导出拓扑超导电性。在实验上，我们也回顾了一些不同体系中的拓扑超导近邻效应的研究进展。文章的第一部分，我们介绍了一些异质结，包括：三维拓扑绝缘体 Bi_2Se_3 和 Bi_2Se_3 与 s 波超导体 $NbSe_2$ 以及 d 波超导体 $Bi_2Sr_2CaCu_2O_{8+\delta}$ 的异质结，拓扑绝缘体 $Sn_{1-x}Pb_xTe$ 与 Pb 的异质结，二维拓扑绝缘体 WTe_2 与 $NbSe_2$ 的异质结。此外，还介绍了 $TiBiSe_2$ 在 Pb 上的拓扑绝缘近邻效应。另一部分中，我们对基于拓扑绝缘体的约瑟夫森结进行了回顾，包括著名的基于 Fu-Kane 体系的拓扑绝缘体约瑟夫森结，以及基于约瑟夫森结的超导量子干涉器件。

关键词：近邻效应；拓扑超导体；异质结；约瑟夫森结